J. Fluid Mech. (2005), *vol.* 524, *pp.* 263–303.
DOI: 10.1017/S0022112004002381 Printed in the United Kingdom

Convective and absolute electrokinetic instability with conductivity gradients

By CHUAN-HUA CHEN, HAO LIN, SANJIVA K. LELE AND JUAN G. SANTIAGO

Department of Mechanical Engineering, Stanford University, Stanford, CA 94305, USA

(Received 16 November 2003 and in revised form 24 August 2004)

Electrokinetic flow instabilities occur under high electric fields in the presence of electrical conductivity gradients. Such instabilities are a key factor limiting the robust performance of complex electrokinetic bio-analytical systems, but can also be exploited for rapid mixing and flow control for microscale devices. This paper reports a representative flow instability phenomenon studied using a microfluidic T-junction with a cross-section of 11 μm by 155 μm. In this system, aqueous electrolytes of 10:1 conductivity ratio were electrokinetically driven into a common mixing channel by a steady electric field. Convectively unstable waves were observed with a nominal threshold field of $0.5\,\mathrm{kV\,cm^{-1}}$, and upstream propagating waves were observed at $1.5\,\mathrm{kV\,cm^{-1}}$. A physical model has been developed for this instability which captures the coupling between electric and flow fields. A linear stability analysis was performed on the governing equations in the thin-layer limit, and Briggs–Bers criteria were applied to select physically unstable modes and determine the nature of instability. The model predicts both qualitative trends and quantitative features that agree very well with experimental data, and shows that conductivity gradients and their associated bulk charge accumulation are crucial for such instabilities. Comparison between theory and experiments suggests the convective role of electro-osmotic flow. Scaling analysis and numerical results show that the instability is governed by two key controlling parameters: the ratio of dynamic to dissipative forces which governs the onset of instability, and the ratio of electroviscous to electro-osmotic velocities which governs the convective versus absolute nature of instability.

1. Introduction

Over the past fifteen years, integrated electrokinetic microsystems have been developed with a variety of functionalities including sample pretreatment, mixing and separation (Reyes *et al.* 2002). These systems are a primary component of so-called micro total analysis systems (μTAS) which aim to integrate multiple chemical analysis functions onto microfabricated chip systems (Manz, Graber & Widmer 1990). As system-level designs increase in complexity, robust control of electrokinetic processes with heterogeneous samples becomes critical. One important regime is on-chip biochemical assays with high conductivity gradients, which might occur intentionally as in sample stacking processes, or unavoidably as in multi-dimensional assays. Such conductivity gradients may lead to an instability under high electric field as shown in this paper. Despite the general lack of literature on electrokinetic instability, it is believed to have been observed by many laboratories (Ramsey 2001), and fragments of anecdotal evidence can be found throughout the literature (see

for example, Shultz-Lockyear *et al.* 1999; Oddy, Mikkelsen & Santiago 2001; Dang *et al.* 2003). As noted in one study of a capillary electrophoresis assay using field amplified sample stacking (FAS): 'once the ionic strength mismatch ... reached a critical threshold ... further increase deteriorated the effect of FAS, resulting in a surprising decrease in separation efficiency and peak distortion,' (Dang *et al.* 2003).

As we will discuss in this paper, electrokinetic instability can be treated as a specialized form of electrohydrodynamic instability which is coupled with electro-osmotic flow. Electrohydrodynamic instability has been a subject of extensive research since Taylor and Melcher's pioneering leaky dielectric model (Melcher & Taylor 1969; Saville 1997). The core of the leaky dielectric model is the Ohmic model, and the essence of the electrohydrodynamic instability mechanism is charge accumulation at material interfaces and its coupling to fluid motion through electric body forces (see, for example, Melcher & Schwartz 1968; Hoburg & Melcher 1976). The natural velocity scale in this instability is the electroviscous velocity that results from a balance between the viscous and electric stresses (Melcher 1981).

The Taylor–Melcher model was originally derived for electrohydrodynamic flow of leaky dielectrics in conventional large-scale systems. This Ohmic model must be modified for electrokinetic microsystems. Specifically, the charge relaxation process is nearly instantaneous for electrolytes and is neglected, and molecular diffusion becomes very important in the microscale regime and is included. In Melcher (1981), two approaches were adopted in deriving the Ohmic model: one approach is based on conservation laws of bulk properties including charge density and electrical conductivity (Melcher & Taylor 1969); the other approach starts from the electro-diffusion equations of individual species which incorporates the Nernst–Plank equations for charged ions (Levich 1962). A proper modification of the Ohmic model for electrokinetic microsystems can be shown using either approach. Despite the recommendation of Melcher (1981), the latter approach has been more popular in the study of electro-convection of electrolytes (e.g. in electrolytic cells). In the electro-convection literature, electro-neutrality is assumed in the derivation of the equivalent of the electrolytic Ohmic model, but the electric body force term is kept in the momentum equation (Levich 1962; Newman 1972). This seemingly counterintuitive electro-neutrality assumption is supported by proper scaling analysis as presented in this paper. Physically, the electro-neutrality assumption is accurate because the difference in cationic and ionic concentrations is very small compared to the background concentration of electrolytes, but this (albeit small) difference is strong enough to promote instability via electric body forces.

In this paper, we will also show that electro-osmotic flow in electrokinetic systems leads to convective and absolute instability. The latter sets in when the internally generated electroviscous velocity disturbances are high enough to overcome electro-osmotic convection. Both the electroviscous and electro-osmotic velocities result from balancing electric body forces and viscous stresses. However, the electroviscous velocity is due to the accumulated net charge density in the bulk (Melcher 1981), whereas the electro-osmotic velocity is due to the net charge within the electric double layer at the boundary (Hunter 1981).

In an open flow system as in the case of convective flow due to electroosmosis, an unstable flow can be classified into two types: convective and absolute (Huerre & Rossi 1998; Schmid & Henningson 2001). Consider a disturbance introduced at a localized point in space: if it grows only downstream, the system is convectively unstable; if the disturbance grows both downstream and upstream, the system is absolutely unstable. Physically, a convectively unstable system is a noise amplifier

in which a disturbance at the origin is amplified downstream, while an absolutely unstable system is an intrinsic oscillator in which the downstream propagating wave oscillates with an upstream propagating wave (Huerre & Rossi 1998). The onset condition of convective instability is the same as that of a temporal instability in which a global disturbance grows in time (Schmid & Henningson 2001). A system that is unstable in a temporal framework can be either convectively or absolutely unstable in the spatial framework. The onset of absolute instability is indicated by a saddle point (Briggs 1964; Bers 1983) or a cusp point (Huerre & Monkewitz 1985; Huerre & Rossi 1998) in the complex dispersion relationship. Such singularities physically correspond to an intrinsic oscillation in which the instability waves have a zero group velocity. The convective versus absolute nature of an instability can be determined by applying the Briggs–Bers criteria to the dispersion relationship between temporal frequency and spatial wavenumber (Schmid & Henningson 2001).

In this paper, we report experimental investigation, analytical modelling and numerical analysis of an electrokinetic flow instability at a microfluidic T-junction. We have presented brief communications of our experimental and theoretical work in previous conference papers. For example, we have experimentally identified electrokinetic instability with a threshold electric field in high-conductivity gradient flows (Chen & Santiago 2002*a*), and identified conductivity gradient and charge accumulation at conductivity interfaces as the key instability mechanism (Chen *et al.* 2003). The current paper presents a more rigorous and complete account of our combined experimental and theoretical study of this new phenomenon. We have adopted the spatial framework for linear stability analysis as motivated by the experimental observation. The spatial framework also helps in determining the nature of instability and unfolding the physics of the instability. See Lin *et al.* (2004) for a temporal stability analysis and nonlinear simulation of a similar instability phenomenon.

We have chosen the terminology 'electrokinetic instability' because of its relevance to electrokinetic microsystems and the important role of electro-osmotic flow in determining the convective nature of such instabilities. However, we stress that the instability originates in the bulk electrolyte (at the conductivity interface) and not in the electric double layer.

The paper is structured as follows. Section 2 presents the experimental set-up and data which motivate the subsequent theoretical work. Section 3 presents a derivation of the Ohmic model for electrolytic solutions. Section 4 presents the linearized thin-layer governing equations that model the high-aspect-ratio experimental system, and the scaling analysis that yields controlling parameters for the instability. Section 5 presents the linear stability analysis based on our model. Section 6 presents numerical results including the onset conditions for convective and absolute instability, and the influence of conductivity profile and non-uniform electro-osmotic flow (due to a dependence of zeta potential on ionic concentration) on the instability dynamics. Section 7 discusses the physics of electrokinetic instabilities. The conductivity-gradient-induced instability mechanism is revealed through a simplified analytical solution, and controlling parameters for the convective and absolute instability are discussed via a systematic parametric variation. Section 8 compares numerical results with experimental data and suggests future work. Section 9 concludes the paper. Appendix A presents the asymptotic derivation of the thin-layer governing equations. Appendix B presents details of the numerical solution. Appendix C presents the application of Briggs–Bers criteria for the selection of physically unstable modes and for the determination of the convective versus the absolute nature of instability.

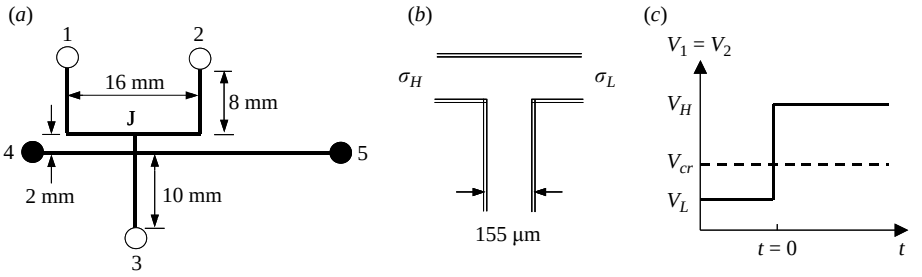

FIGURE 1. Schematic of the experimental set-up. (*a*) Chip design: solid lines represent microfluidic channels with a cross-section of 11 μm × 155 μm. Open circles represent fluid reservoirs filled with approximately 2×10^{-7} m^3 working fluid of appropriate conductivies. Solid circles represent seals on side channels. The same voltage is applied to reservoirs R1 and R2 ($V_1 = V_2$), and R3 is grounded ($V_3 = 0$). The T-junction region (from reservoirs R1 and R2 to R3) has a nominal length of 2 cm, where the symmetric Ts (R1–J and R2–J) contribute to a total effective channel length of 8 mm. (*b*) T-junction schematic with the region near joint 'J' in (*a*) enlarged. Buffer streams of 10 : 1 ($\sigma_H : \sigma_L$) conductivity ratio are electrokinetically driven to the mixing channel, i.e. from R1 and R2 to R3. (*c*) Typical voltage scheme: a relatively low voltage (V_L) is first used to establish a stable flow and conductivity field. At time $t = 0$, the voltage is raised to V_H which is above the threshold value of instability (V_{cr}).

2. Experiments

2.1. *Experimental set-up*

The chip layout is shown in figure 1(*a*). The microfluidic chip was fabricated on glass substrates using standard microlithographic wet etching and thermal bonding techniques. The fabrication steps of a similar system were described in a previous paper (Chen & Santiago 2002*b*), note that a slightly higher bonding temperature of 600 °C was used here for fusion bonding of borofloat glass substrates (Precision Glass & Optics, Santa Ana, CA, USA). This chip was also designed to perform electrokinetic binding assays as described by Chen (2004); Matta *et al.* (2004). For the experiments reported here, the two ends (R4 and R5) in figure 1(*a*) were sealed with chromatography fittings after being filled with buffer of appropriate conductivities, so only the T-junction (at point 'J') in this figure was important to these experiments. The mixing channel cross-section is 11 μm deep and 155 μm wide. The nominal length of the T-junction is 2 cm. Note that nominal electric fields in the mixing (outlet) channel were approximated by assuming the conductivity in this channel (J–R3) to be equal to the arithmetic average conductivity of the inlet streams.

As shown in figure 1(*b*), 10 mol m^{-3} and 1 mol m^{-3} (or 10 mM and 1 mM) borate buffers (CAS registry 81-88-9, Acros Organics, NJ, USA) were introduced into reservoirs R1 and R2, respectively. The molar conductivity was measured as 7.7×10^{-3} S m^2 mol^{-1}. The 10 mM buffer was seeded with 0.1 mM rhodamine B (CAS 1303-96-4, J. T. Baker, NJ, USA) which is reported to be neutral for pH values ranging from 6.0 to 10.8 (Schrum *et al.* 2000). The ionic concentrations were low enough such that the permittivity and viscosity were the same as that of pure water (see, for example, Pottel 1973; Horvath 1985). The ionic diffusivities were obtained as follows: the tabulated molar conductivity of Na^+ is 5.0×10^{-3} S m^2 mol^{-1}, and diffusivity is 1.3×10^{-9} m^2 s^{-1} (Lide 1996). The molar conductivity of $B(OH)_4^-$ was estimated to be 2.7×10^{-3} S m^2 mol^{-1} based on the difference between the total molar conductivity and that of Na^+ ions. For a dilute solution, molar conductivity is linearly proportional

to ionic mobility and (by Einstein's relation) to diffusivity (Levich 1962), hence the diffusivity of $B(OH)_4^-$ was estimated to be $0.70 \times 10^{-9}\,m^2\,s^{-1}$.

Figure 1(*c*) shows the voltage scheme used in the experiments. A relatively low voltage was applied to establish the interface between the two streams. At time $t = 0$, a voltage higher than the critical voltage was applied to produce instability waves. The voltage step was created by a high-voltage switching unit equipped with mechanical relays with 2 ms temporal resolution (Micralyne, Alberta, Canada).

Fluorescence images were collected using an inverted microscope (Nikon TE300, Tokyo, Japan) with a 10× objective (NA = 0.3), a 0.5× demagnification lens (to increase field of view), and a high-frame-rate four-chip CCD camera (Pluto12, Pixelvision, Tigard, OR, USA). The exposure time was 10 ms and sampling frequency was 50 Hz. Preliminary experiments were performed using 10, 50, 80 and 200 Hz sampling frequencies (using various pixel binning strategies) and 2–10 ms exposure times in order to verify that the images presented here are not aliased.

2.2. *Experimental results*

High conductivity ratio is a critical parameter for the electrokinetic instabilities we have observed (Chen & Santiago 2002*a*; Lin *et al.* 2004). In the current set-up, we visualized homogeneous flow cases with 1 : 1 conductivity ratio at 10 mM or 1 mM, and verified that both of these flow conditions were stable at all applied voltages (0–3 kV). In contrast, the 10 : 1 conductivity ratio case clearly shows unstable behaviour above a threshold electric field.

Figure 2 shows time series images of convective instability waves at various electric fields. Figure 2(*a*) shows a stable flow field with fluorescent dye established using a relatively low voltage of 0.5 kV, corresponding to a nominal electric field $E_a = 0.25\,kV\,cm^{-1}$ which is defined here as the voltage drop divided by the nominal length of 2 cm. At time $t = 0$, higher voltages were applied and unstable waves appeared within 5 ms (determined by maximum temporal resolution of the camera) above a nominal threshold of $0.5 \pm 0.1\,kV\,cm^{-1}$. The threshold condition was determined by the lowest voltage at which the flow behaviour was visibly different from the base state (e.g. with periodic structures growing and advecting downstream). In one particular realization at $0.5\,kV\,cm^{-1}$, a very slight disturbance was observed (figure 2*b*), e.g. the point of median intensity fluctuates up to 10% (peak-to-peak) of the channel width at three channel widths downstream. This disturbance was more obvious at $0.75\,kV\,cm^{-1}$ (figure 2*c*). Above $1\,kV\,cm^{-1}$, instability wave structures were apparent in the experimental visualization (figure 2*d*, *e*). Disturbances typically originate at a stationary point and grow as they advect downstream.

Figure 3 shows evidence of the presence of absolute instability waves. At a nominal electric field of $1.5\,kV\,cm^{-1}$, the upstream flow region (near the wall on the left-hand side) was visibly perturbed (figure 3*b*). This upstream disturbance is attributed to the upstream propagation of disturbances originating near the entrance of the mixing channel. Note that the wave structure broke down and lost regularity at this high field (figure 3*a*).

Figure 4 shows the speed of initial disturbance propagation as a function of electric field. The speed is obtained by tracking the wavefront ('valley') of the initial disturbance, and is a measurement of the group velocity (v_g) of the unstable waves. Take figure 2(*e*) at $1.25\,kV\,cm^{-1}$ as an example, from 0.1 s to 0.5 s the disturbance traveled approximately 1.5 channel widths, or $3h$ where h is the half-width of the mixing channel. This measurement corresponds to a speed of $1.1\,mm\,s^{-1}$. As shown in figure 4, the measured propagation speed is a linear function of the electric field

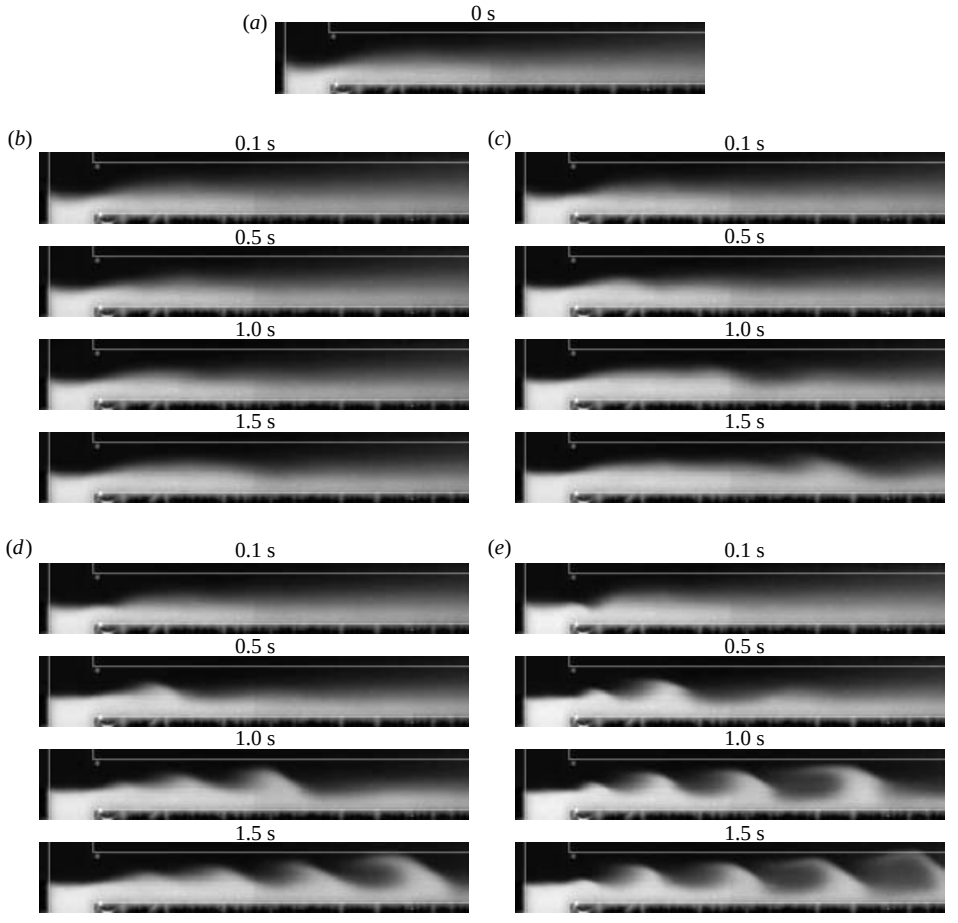

FIGURE 2. Time series images of convective instability waves. (*a*) Borate buffers of 1 mM and 10 mM are introduced at a stable electric field 0.25 kV cm^{-1}. The high-conductivity stream is seeded with neutral fluorescent dye. (*b–e*) Images at increasing electric field, (*b*) 0.5, (*c*) 0.75, (*d*) 1.0, (*e*) 1.25 kV cm^{-1}. In each case, the disturbance originates in the intersection region ($t = 0.1$ s) and is convected downstream ($t = 0.5$–1.5 s). The strength of the disturbance increases with increasing electric field.

for the convectively unstable waves. This observation suggests that electro-osmotic flow is carrying the waves downstream in the convective instability regime.

As a confirmation to the convective role of electro-osmotic flow, the average electro-osmotic velocity at the conductivity interface was measured at a stable field of 0.25 kV cm^{-1}. A localized disturbance was introduced by a brief voltage spike, where applied voltage was raised from 0.5 kV up to 2 kV (above the instability threshold) and then back to 0.5 kV after approximately 20 ms. This brief spike introduced a small disturbance in the scalar field in the flow region near the centreline. The velocity of this disturbance was then tracked in subsequent images and measured to be 0.25 ± 0.05 mm s^{-1} at 0.25 kV cm^{-1}, consistent with a linearly extrapolated group velocity of 0.24 mm s^{-1} from figure 4.

The amplitude and spatial extent of disturbances increased with electric field as shown in figure 2. This trend is also evident in the root mean square (r.m.s.) images of the scalar concentration field as shown in figure 5. As the electric field was increased,

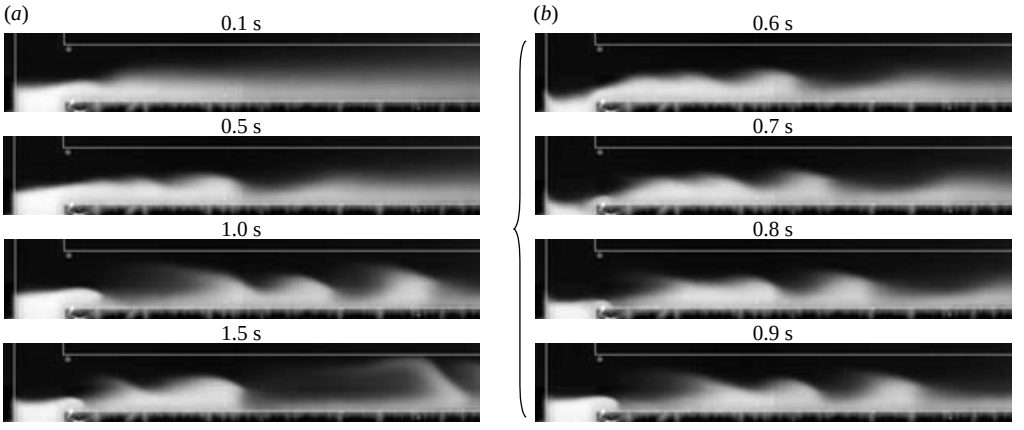

FIGURE 3. Time series images indicating absolute instability at 1.5 kV cm^{-1}. (*a*) Snapshots at 0.5 s intervals: at high field, the regular wave structure breaks down. (*b*) Details of temporal evolution in the range $t = 0.6$–0.9 s: the region upstream of the inlet of the mixing channel is strongly perturbed. The initial condition at time $t = 0$ is the same as shown in figure 2(*a*). The high-conductivity stream is seeded with neutral fluorescent dye.

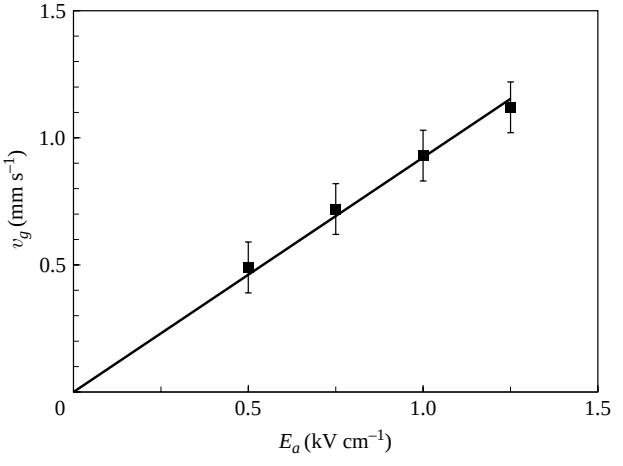

FIGURE 4. Speed of initial disturbance propagation. The 'valley' of the wavefront is tracked to measure the group velocity (v_g). The propagation speed is correlated with electro-osmotic flow velocity as both are linearly proportional to the applied electric field (E_a). The error bar is based on twice the standard deviation of three realizations at 1.0 kV cm^{-1}.

the strongly perturbed region appeared to shift toward the high conductivity side, and the initial disturbances appeared to originate further upstream. In the convective regime (figure 5*a–c*), the perturbation was asymmetrical and the low-conductivity side was perturbed more than the high-conductivity side. In the case of absolute instability (*d*), however, the scalar perturbation was stronger on the high-conductivity side, and the intersection region was strongly disturbed.

The perturbation energy of the scalar field is plotted in figure 6. The scalar perturbation energy En_s is defined here as the mean square value of the scalar intensity, i.e. the square of the r.m.s. intensity which is shown in figure 5. At 0.75–1.25 kV cm^{-1}, the downstream growth of the perturbation energy indicates that the flow was convectively

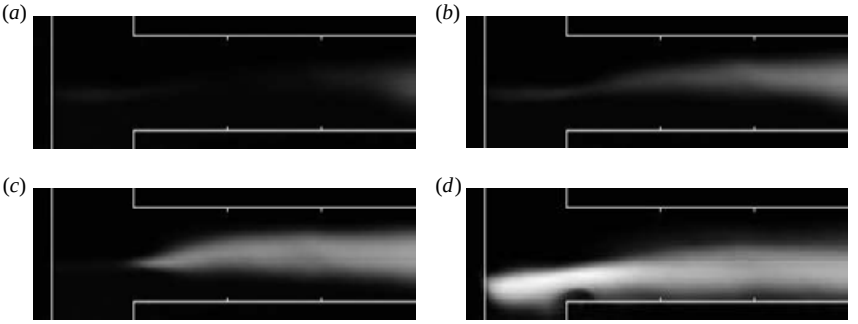

FIGURE 5. The spatial extent of instability as indicated by plots of the root-mean-squared image intensity. (*a*) 0.75, (*b*) 1.0, (*c*) 1.25, (*d*) 1.5 kV cm^{-1}. The intensity here corresponds to the strength of the fluctuation of image intensity, and not to the dye concentration. Images were taken at 50 Hz and the root-mean-squared values were obtained over the following time intervals: (*a*) 0.8–1.5 s; (*b–d*) 0.5–1.5 s. The tick marks correspond to 1, 2 and 3 channel widths (or 2, 4 and 6 h) downstream of the mixing channel entrance.

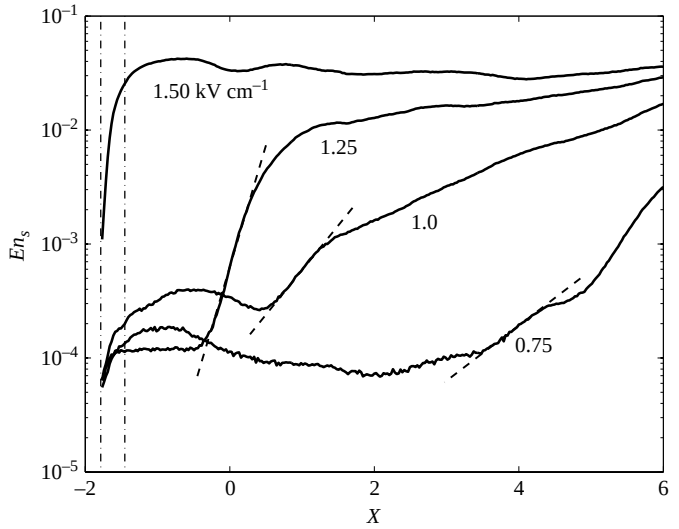

FIGURE 6. Energy of scalar fluctuations. The scalar perturbation energy is the square of the r.m.s. intensity shown in figure 5. At each location (X), the normalized fluctuation energy is averaged over the width of the mixing channel. Each convective instability case (0.75–1.25 kV cm^{-1}) has an exponential growth region for the perturbation energy (indicated by the dashed curves) followed by a slower-growing region. An exception is the absolute instability case (1.5 kV cm^{-1}), which has a nearly constant perturbation energy. Note the width of the T-channels is slightly smaller than the mixing channel. The left-most vertical dot-dashed line represents the position of the wall. The region between the two dot-dashed lines corresponds to the region immediately adjacent to the left-most vertical channel wall, where small values of perturbation are observed. The downstream location (with respect to the entrance of the mixing channel, see also caption of figure 5) is non-dimensionalized by the channel half-width h. The scalar intensity is corrected for non-uniform illumination and camera response using dark and flat field images. A flat field image of 0.1 mM rhodamine B is also used to normalize the image intensity.

unstable. At 1.5 kV cm^{-1}, however, the perturbation energy was relatively constant over most of the flow field, supporting the case that the flow at this high field was absolutely unstable. For the convectively unstable cases (particularly at 1.0,

	Onset	Convective instability			Absolute	Notes
E-field ($kV\,cm^{-1}$)	0.5	0.75	1	1.25	1.5	Nominal length is 2 cm
Growth rate (h^{-1})	$\simeq 0$	0.2 ± 0.2	0.4 ± 0.2	1.1 ± 0.4	–	Fit to perturbation energy
Frequency (Hz)	$\simeq 0$	0.8 ± 0.8	2.7 ± 1.2	3.9 ± 0.8	2.3 ± 1.6	Pointwise Fourier analysis

TABLE 1. Experimental measurement of spatial growth rate and temporal frequency. The error bars in growth rate are based on twice the standard deviations of three realizations at $1.0\,kV\,cm^{-1}$. The error bars in frequency are based on the minimum frequency resolution with 64 data points sampled at 50 Hz. A Hanning window was applied in all spectral analyses to reduce frequency leakage.

$1.25\,kV\,cm^{-1}$), the perturbation energy initially grew exponentially, and then grew at a decreased growth rate. The exponential growth region is consistent with the linear stability theory in which the scalar perturbation energy (En_s) grows proportionally as $\exp(-2K_i X)$, where the growth rate ($-K_i$) and streamwise location X are both non-dimensionalized by the channel half-width (h). In order to compare these data to the linear model, we estimated the spatial growth rates for the convective cases by the exponent of the $En_s - X$ curve in the exponential growth regions, see figure 6 and table 1 for details.

In addition to group velocity and spatial growth rate, the measurable characteristics of the instability waves include temporal frequency, wavelength and phase speed. Temporal frequency was determined using a Fourier analysis of the fluctuating scalar intensity at a spatially fixed point. This fixed point was chosen at the centreline of the mixing channel and one channel width downstream of the T-intersection ($X = 2$). Table 1 gives the measured frequencies. The frequency increased with increasing electric field in the convective instability regime. However, this trend does not hold in the absolute instability regime. For example, the maximum-spectral-power frequency of 2.3 ± 1.6 Hz at $1.5\,kV\,cm^{-1}$ was lower than the frequency of 3.9 ± 0.8 Hz at $1.25\,kV\,cm^{-1}$. The convective instability waves were dispersive. Wavelengths increased from approximately one channel width ($2h$) to two channel widths as waves propagated downstream and interacted with the sidewalls. At a given downstream location, however, wavelengths were nearly constant for electric fields ranging from 0.75 to $1.25\,kV\,cm^{-1}$. Phase speed also increased as the waves propagated downstream. The phase speed appeared to approach the propagation speed of the initial disturbance (see figure 4) when the wavelength grew to approximately two channel widths. Like the group velocity, the phase speed was also proportional to electric field, which also suggests that the electro-osmotic flow acts as a convecting medium.

3. Ohmic model for electrolytic solutions

In this section, the Ohmic model for electrolyte solutions is derived as an extension of that of Levich (1962). Similar models have been adopted in the study of the electro-diffusion process of electrolytes in different physical regimes (see, for example Newman 1972; Rubinstein 1990). Lin *et al.* (2004) presented a simplified version of this electrolytic Ohmic model assuming binary electrolyte with symmetric properties. We shall present a brief derivation of this model and discuss the two assumptions behind the model: electro-neutrality and negligible diffusive current. Our derivation is along the line of Levich (1962); see Newman (1972) for a somewhat different perspective.

For a monovalent binary electrolyte which is fully dissociated, charge density (ρ_f) and electric conductivity (σ) are related to concentration of cations (c_+) and anions (c_-) through (Levich 1962; Probstein 1994)

$$\rho_f = F(c_+ - c_-), \tag{3.1}$$

$$\sigma = F^2(c_+ m_+ + c_- m_-), \tag{3.2}$$

where F is the Faraday constant, m is ionic mobility (in mol s kg^{-1}). Electro-neutrality can be assumed to simplify the problem in the limit of

$$\Theta = F m_+ \frac{\rho_f}{\sigma} = \frac{c_+ - c_-}{c_+ + \frac{m_-}{m_+} c_-} \ll 1, \tag{3.3}$$

where Θ represents the ratio of cationic and anionic concentration difference (which contributes to the charge density) to the total concentration of ions (which contributes to the electrical conductivity). Physically, the electro-neutrality assumption holds when the difference in cationic and ionic concentrations is very small compared to the background concentration of electrolytes. Under electro-neutrality, $c_+ = c_- = c$ where c is the reduced ionic concentration, and conductivity is proportional to this reduced ionic concentration by

$$\sigma = F^2(m_+ + m_-)c. \tag{3.4}$$

Assuming electro-neutrality, the conservation equations of charged species can be combined to yield (Levich 1962, pp. 278–286),

$$\frac{\partial c}{\partial t} + (\boldsymbol{v} \cdot \nabla)c = D_{eff} \nabla^2 c, \tag{3.5a}$$

$$\nabla \cdot \boldsymbol{i} = 0, \tag{3.5b}$$

where $\boldsymbol{v}$ is fluid velocity. The effective diffusivity D_{eff} is defined as

$$D_{eff} = \frac{2D_+ D_-}{D_+ + D_-}, \tag{3.6}$$

where $D_\pm$ is ionic diffusivity, and is related to mobility by Einstein's relation $D_\pm = RTm_\pm$ where R is the universal gas constant, and T is temperature. Current density $\boldsymbol{i}$ is related to reduced concentration by

$$\boldsymbol{i} = \boldsymbol{i}_O + \boldsymbol{i}_D = F^2(m_+ + m_-)c\boldsymbol{E} - F(D_+ - D_-)\nabla c, \tag{3.7}$$

where $\boldsymbol{E}$ is electric field. Ohmic current $\boldsymbol{i}_O$ is due to electro-migration of both ions, while diffusive current $\boldsymbol{i}_D$ is due to competing diffusion of cations and anions. Note convection current $\boldsymbol{i}_C = \rho_f \boldsymbol{v} = 0$ under the electro-neutrality assumption. Invoking the Einstein relation, the order of magnitudes of diffusive current and conductive current are compared as,

$$\frac{\boldsymbol{i}_D}{\boldsymbol{i}_O} \sim O\left(\frac{D_- - D_+}{D_+ + D_-} \frac{RT/F}{E_a \delta} \frac{\Delta c}{c_{avg}}\right) = \frac{E_d}{E_a}, \tag{3.8}$$

where E_a is the applied electric field, RT/F is the thermal voltage (25.7 mV at 25 °C), Δc is the concentration change over a diffusion length of δ, c_{avg} is the average concentration, and E_d is the diffusion electric field (Levich 1962, p. 286) due to the unequal diffusivities of anions and cations. Here symbol '$O(\ )$' denotes the order of magnitude of a variable. The diffusivities of small ions are usually similar. In the case

of borate buffer, the diffusivities of cations (Na^+) and anions ($B(OH)_4^-$) are within a factor of two. For the system of interest to us,

$$\frac{\Delta c}{c_{avg}} \sim O\left(\frac{\sigma_H - \sigma_L}{\sigma_H + \sigma_L}\right) = \frac{\gamma - 1}{\gamma + 1} < 1, \tag{3.9}$$

where $\gamma = \sigma_H/\sigma_L$ is the ratio of high to low conductivity. Under our experimental condition, $E_a \sim O(10^5)\,\mathrm{V\,m^{-1}}$ and $\delta \sim O(10^{-5})\,\mathrm{m}$, therefore $\boldsymbol{i}_D/\boldsymbol{i}_O \sim O(10^{-2})$ and the diffusive current can be neglected for the present analysis. Physically, the diffusive current can be neglected when the diffusive electric field, $E_d \sim O(10^3)\,\mathrm{V\,m^{-1}}$ under the above conditions, can be neglected in comparison with the applied electric field which is of order $O(10^5)\,\mathrm{V\,m^{-1}}$. Since the convection current is zero under the electro-neutrality assumption, electrical current can be assumed to be dominated by Ohmic current,

$$\boldsymbol{i} \simeq \boldsymbol{i}_O = \sigma \boldsymbol{E}. \tag{3.10}$$

The Ohmic model for electrolytic solutions is obtained by assuming electro-neutrality and negligible diffusive current. Applying the linear relationship between reduced concentration and conductivity (3.4), equations (3.5) reduce to

$$\frac{\partial \sigma}{\partial t} + (\boldsymbol{v} \cdot \nabla)\sigma = D_{eff} \nabla^2 \sigma, \tag{3.11a}$$

$$\nabla \cdot (\sigma \boldsymbol{E}) = 0. \tag{3.11b}$$

Under electro-neutrality, the electrical conductivity can be viewed as a material property which obeys a convective diffusion equation, (3.11*a*). Equation (3.11*b*) is simply Kirchhoff's Law valid for the special case where Ohmic current dominates.

Once the electrolytic Ohmic model is obtained, charge density can be estimated using Gauss' law

$$\nabla \cdot (\epsilon \boldsymbol{E}) = \rho_f, \tag{3.12}$$

where ϵ is fluid permittivity. The current continuity equation, (3.11*b*), is rearranged as,

$$\rho_f = -\epsilon \boldsymbol{E} \cdot \nabla \sigma / \sigma. \tag{3.13}$$

It is important to note that electrical conductivity is not a passive scalar because a change in conductivity will alter the electric field and induce net charge, and the resulting electric body force will alter the velocity field. Equation (3.13) suggests that charge density scales as

$$\rho_f \sim \Gamma \epsilon E_a / \delta, \tag{3.14}$$

where Γ accounts for the effect of conductivity gradients. As shown in the subsequent linear scaling analysis, $\Gamma = (\gamma - 1)^2/(\gamma + 1)^2$ is of order unity or less (similar to (3.9)). Note ρ_f is scaled by the net charge required to maintain conservation of ionic current at the conductivity interface. We can now check for the consistency of the electro-neutrality assumption. Applying (3.14),

$$\Theta = Fm_+ \frac{\rho_f}{\sigma} \sim O\left(\frac{D_+}{kT/e} \frac{\Gamma \epsilon E_a/\delta}{\sigma_r}\right), \tag{3.15}$$

where σ_r is a reference conductivity which is chosen as the average conductivity. Under our experimental condition, the parameter scales are $D_+ \sim O(10^{-9})\,\mathrm{m^2\,s^{-1}}$, $E_a \sim O(10^5)\,\mathrm{V\,m^{-1}}$, $\delta \sim O(10^{-5})\,\mathrm{m}$, and $\sigma_r \sim O(10^{-2})\,\mathrm{S\,m^{-1}}$, therefore, $\Theta \sim O(10^{-4})$ and electro-neutrality is an excellent approximation for our systems.

Equations (3.11*a*) and (3.11*b*) constitute the Ohmic model for electrolytic solutions. It is interesting to compare these equations to the classic Ohmic model derived by Melcher, which is applicable for leaky dielectrics in the context of electrohydrodynamics (Melcher 1981). Our model differs from Melcher's Ohmic model in two ways. First, our model includes a diffusive term for conductivity. This diffusive term is important because our model is 'bulk-coupled' in that diffusion sets up the base state (Hoburg & Melcher 1976) and, more importantly, diffusion stabilizes the flow and is critical for capturing the threshold electric field (Baygents & Baldessari 1998). Secondly, our model neglects the charge relaxation processes. The charge relaxation time scale ($\tau_e = \epsilon/\sigma$) for electrolyte systems is typically less than 10 μs, very short compared to the time scales of interest. We therefore assume instantaneous charge relaxation (Hoburg & Melcher 1976) in order to eliminate unnecessary numerical stiffness. Including the diffusive term and neglecting the charge relaxation process are important for electrokinetic microsystems as compared to conventional electrohydrodynamic systems, because the former have smaller length scales (typically $\leqslant 10^{-4}$ m, *vs.* $\geqslant 10^{-2}$ m for electrohydrodynamics) and higher conductivity (typically $\geqslant 10^{-4}$ S m^{-1}, *vs.* $\leqslant 10^{-9}$ S m^{-1} for electrohydrodynamics).

4. Governing equations

The conductivity distribution and electric field are governed by the electrolytic Ohmic model, and the fluid motion is governed by the incompressible Navier–Stokes equations,

$$\frac{\partial \sigma}{\partial t} + (\boldsymbol{v}\cdot\nabla)\sigma = D_{eff}\nabla^2\sigma, \tag{4.1a}$$

$$\nabla\cdot(\sigma\nabla\phi) = 0, \tag{4.1b}$$

$$\nabla\cdot\boldsymbol{v} = 0, \tag{4.1c}$$

$$\rho\frac{\partial \boldsymbol{v}}{\partial t} + \rho(\boldsymbol{v}\cdot\nabla)\boldsymbol{v} = -\nabla p + \mu\nabla^2\boldsymbol{v} + \epsilon(\nabla^2\phi)\nabla\phi, \tag{4.1d}$$

where ρ is mass density, p is pressure and μ is the dynamic viscosity of the working liquid. The electric field is assumed to be quasi-static and is related to electric potential ϕ by $\boldsymbol{E} = -\nabla\phi$. Note that the electric body force term in the momentum equation couples the electric and flow fields. The absolute temperature rise in our system is estimated to be less than 2 °C and the temperature difference in our channel is estimated at less than 1 °C;† we therefore assume constant temperature in our model.

Two velocity scales are necessary to properly scale the various terms in the governing equations. The electro-osmotic velocity is an apparent velocity scale due to the net charge in the electric double layer (close to the wall), and is introduced as part of the boundary conditions. The electroviscous velocity is the internal scale for velocity disturbances due to net charge accumulation in the bulk, i.e. within the diffusive conductivity interface. The electroviscous velocity is first derived heuristically, then confirmed with a rigorous asymptotic analysis of the linearized governing equations. By judiciously applying these two velocity scales, the linearized governing equations are non-dimensionalized. The scaling analysis presented in this section will be further supported by numerical results in §§6–7.

† The temperature rise is estimated according to the experimentally validated Joule heating model by Swinney & Bornhop (2002) for a similar system (see equation 1 of this reference).

4.1. *Boundary conditions and base state*

In this paper, we assume the physics of the electric double layer influences the instability dynamics only in that the double layer determines an electro-osmotic velocity very close to the microchannel wall. This assumption is supported by the fact that the electric double layers of interest here have a characteristic Debye length (λ_D) which is less than 10 nm (Hunter 1981), and is much smaller than the characteristic channel dimensions.† The boundary conditions are therefore,

$$\boldsymbol{n}\cdot\nabla\sigma = 0, \tag{4.2a}$$

$$\boldsymbol{n}\cdot\nabla\phi = 0, \tag{4.2b}$$

$$\boldsymbol{v} = -\epsilon\zeta\nabla\phi/\mu, \tag{4.2c}$$

where $\boldsymbol{n}$ denotes wall-normal direction, and ζ is the zeta potential of the electrical double layer. Boundary conditions (4.2*a*) and (4.2*b*) are consequences of non-penetrating walls. The electro-osmotic velocity at the wall is a function of local concentration and electric field, and is given by the Smoluchowski equation (4.2*c*) (Hunter 1981). In our thin-double-layer electrolyte system, the plane at which the electro-osmotic velocity condition (4.2*c*) is posed can support both a non-zero velocity and a shear stress (Santiago 2001); this plane is only a few Debye lengths away from the wall and can be assumed to be collocated with the physical walls (Hunter 1981).

Zeta potential is related to ionic concentration, which is proportional to ionic conductivity for dilute solutions under the electro-neutrality condition (equation (3.4)). The following correlation is assumed

$$\frac{\zeta}{\zeta_r} = \left(\frac{\sigma}{\sigma_r}\right)^{-n}, \tag{4.3}$$

where n is an empirical constant, and ζ_r is a reference zeta potential at the reference conductivity of σ_r. Although a simple thin-double-layer theory suggests a power law with $n = 1/2$ by assuming constant surface charge (Hunter 1981; Probstein 1994), the dependence is typically much weaker in practice. There is not a generally accepted correlation between zeta potential and ionic conductivity (concentration). However, existing experimental data suggest that the dependence is approximately $n = 1/4$ for borate buffer in borosilicate glass channels (Yao *et al.* 2003). In the modelling work below, we shall investigate the influence of various empirical relations ($n = 0, 1/4, 1/2$) on the instability dynamics.

Figure 7 schematically shows the idealized system of interest. The conductivity interface is assumed to be uniform, and the base diffusive conductivity profile is approximately

$$\sigma_0 = \sigma_L + \frac{\sigma_H - \sigma_L}{2}\mathrm{erfc}\left(\frac{y}{\delta}\right). \tag{4.4}$$

The base state is assumed parallel, i.e.

$$\sigma_0 = \sigma_0(y), \quad \boldsymbol{E}_0 = E_a\boldsymbol{e}_x, \quad p_0 = 0, \quad \boldsymbol{v}_0 = u_0(y)\boldsymbol{e}_x, \tag{4.5}$$

† By this assumption, we have also neglected various higher-order effects within the double layer such as unsteady charging and two-dimensional potential gradients. Bazant, Thornton & Ajdari (2004) discuss transient double-layer physics and Anderson (1989) discusses diffusio-osmosis due to concentration gradient of electrolytes. Order of magnitude estimates show such effects are of secondary importance to our problem; see the cited references for details.

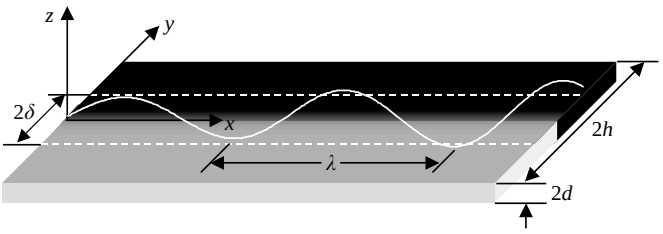

FIGURE 7. Schematic model of the high-aspect-ratio experimental system. The horizontal length scales, including diffusion length 2δ, channel width $2h$, and instability wavelength λ, are assumed to be of the same order. The channel depth $2d$ is much larger than the Debye length, but much smaller than the horizontal length scales. The diffusion length is assumed to be uniform.

where subscript '0' denotes the base state and $\boldsymbol{e}_x$ denotes the unit direction in x. The base electro-osmotic velocity is $u_0 = U_{eo}(\sigma_0/\sigma_r)^{-n}$ by means of equation (4.3), where the reference electro-osmotic velocity U_{eo} at ζ_r is defined by the Smoluchowski equation (Probstein 1994),

$$U_{eo} = \frac{\epsilon \zeta_r E_a}{\mu}. \tag{4.6}$$

See Appendix B.1 for a detailed discussion of the base state.

By assuming a parallel base state, the linear stability analysis is greatly simplified and no boundary conditions are required in the streamwise (x-) direction. In reality, the electrokinetic flow near the T-junction is non-parallel so that, for example, diffusion length increases downstream. The validity of the parallel base state assumption is discussed in § 8.

4.2. *Electroviscous velocity*

Electrokinetic instabilities are largely internally driven processes, as discussed below. The electro-osmotic velocity scale (U_{eo}) governs the apparent convective motion and is not an appropriate scale for internal velocity disturbances. The correct internal velocity scale is the electroviscous velocity scale, U_{ev}, which is obtained by balancing viscous and electric stresses. The electroviscous velocity scale is similar to that defined in Hoburg & Melcher (1976) and Melcher (1981). Our definition strives to account for all the relevant physical parameters involved in the electroviscous balance of our problem.

Motivated by the high-aspect-ratio experimental system schematically shown in figure 7, we shall focus on the asymptotic thin-layer limit where $\varepsilon = d/h \ll 1$, i.e. the channel depth ($2d$) is much thinner than the horizontal length scales which are assumed to be of the same order of the channel width ($2h$). As discussed in § 4.1, the Debye length is assumed to be much smaller than the channel depth ($2d$).

In the thin-layer limit, conductivity (σ) and potential (ϕ) are both independent of z, but velocity ($\boldsymbol{v}$) has a z-dependence. This difference in z-dependence is due to the different boundary conditions of these variables as in (4.2). The walls at $z = \pm d$ prohibit mass or electric fluxes, but accommodate momentum fluxes. The z-dependence of various variables can also be rigorously derived using asymptotic analysis as shown in § 4.3 (and Appendix A).

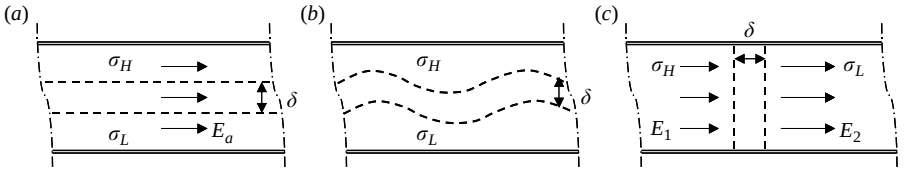

FIGURE 8. Schematic of conductivity interfaces for: (*a*) base state of flow with no net charge, where E_a is the applied electric field; (*b*) perturbed state with bulk charge accumulation, which is bounded by cases (*a*) and (*c*); (*c*) the worst-case scenario in which the conductivity gradient is in the direction of electric field. From current continuity, E_1 on the high-conductivity side is $2E_a/(\gamma+1)$, and E_2 on the low-conductivity side is $2\gamma E_a/(\gamma+1)$. Compared to the base state (*a*), the electric field perturbation in the worst-case scenario (*c*) is $(E_2-E_a)=E_a(\gamma-1)/(\gamma+1)$ on the low-conductivity side, and oppositive in sign on the high-conductivity side.

The key to the scaling analysis is the charge density scale, which is deduced from the linearized form of the current conservation equation, (3.13),

$$\bar{\rho}_f = -\epsilon \bar{\boldsymbol{E}} \cdot \frac{\nabla \sigma_0}{\sigma_0} - \epsilon \boldsymbol{E}_0 \cdot \frac{\nabla \bar{\sigma}}{\sigma_0}, \tag{4.7}$$

where the overbar represents a perturbation quantity (more rigorously, a depth-average perturbation quantity, see § 4.3). In this decomposition, we can classify charge perturbation as arising from (i) the electric field perturbation ($\bar{\boldsymbol{E}}$) in the direction of the base conductivity gradient; and (ii) the gradient of the conductivity perturbation ($\nabla\bar{\sigma}$) in the direction of the base electric field. The scaling of a perturbation variable is more straightforward than that of the gradient of the perturbation. We therefore chose to use the term involving $\bar{\boldsymbol{E}}$ to scale $\bar{\rho}_f$.

As shown in figure 8, for a perturbed state (figure 8*b*), the magnitude of charge density induced by a given conductivity gradient can be bounded by considering two limiting cases. Figure 8(*a*) is the base state with a finite diffusion layer and a conductivity gradient perpendicular to the electric field direction. Figure 8(*c*) shows a perturbed region in the flow with a conductivity gradient parallel to the imposed electric field. The latter case results in the largest value of electric field perturbation $\bar{\boldsymbol{E}}$ and therefore the highest net charge density $\bar{\rho}_f$. As detailed in figure 8, the electric field perturbation scales with this worst-case scenario,

$$\bar{\boldsymbol{E}} \sim O\left(\frac{\gamma-1}{\gamma+1}E_a\right). \tag{4.8}$$

Following arguments similar to (3.8) and (3.9),

$$\frac{\nabla\sigma_0}{\sigma_0} \sim O\left(\frac{(\sigma_H-\sigma_L)/(2\delta)}{(\sigma_H+\sigma_L)/2}\right) = O\left(\frac{1}{\delta}\frac{\gamma-1}{\gamma+1}\right). \tag{4.9}$$

Therefore, charge density scales as

$$\bar{\rho}_f \sim O\left(-\epsilon\bar{\boldsymbol{E}}\cdot\frac{\nabla\sigma_0}{\sigma_0}\right) \sim O\left(\Gamma\frac{\epsilon E_a}{\delta}\right), \tag{4.10}$$

where Γ (together with δ) accounts for the effect of conductivity gradients, and

$$\Gamma = \frac{(\gamma-1)^2}{(\gamma+1)^2}. \tag{4.11}$$

For the high-conductivity gradient system (i.e. $\gamma \gg 1$), $\Gamma \approx 1$.

Balancing the viscous and electric forces in the momentum equation, we then have

$$U_{ev} \sim \frac{\bar{\rho}_f \boldsymbol{E}_0}{\mu/d^2} \sim \Gamma \frac{d^2}{\delta} \frac{\epsilon E_a^2}{\mu}. \tag{4.12}$$

Note δ is the diffusion half-length across which conductivity varies, and is therefore the relevant length scale for charge density. However, d is the relevant length scale for wall-bounded viscous transport.

4.3. *Linearized thin-layer equations*

In order to model the high-aspect ratio experimental system schematically shown in figure 7, we shall adopt the linearized thin-layer governing equations which are derived asymptotically in Appendix A. The main results from this asymptotic analysis are summarized below.

Assuming a one-dimensional parallel base state (4.5), the thin-layer equations are obtained in the high-aspect-ratio limit with $\varepsilon = d/h \ll 1$, where d is channel half-depth and h is the channel half-width. These equations are valid in the low-Reynolds-number ($\varepsilon Re \ll 1$) and low-Péclet-number ($\varepsilon Pe \ll 1$) limit, where $Re = \rho U_{eo} d/\mu$ is the Reynolds number and $Pe = U_{eo} d/D_{eff}$ is the Péclet number.

In the asymptotic limit, the conductivity and potential have no z-dependence at leading order, and the velocity profile is,

$$\boldsymbol{v}'_H = \bar{\boldsymbol{v}}_{ev}(x, y, t) g(z) + \bar{\boldsymbol{v}}_{eo}(x, y, t), \tag{4.13}$$

where subscript H means horizontal direction (e.g. $\bar{\boldsymbol{v}}_H = \bar{u}\boldsymbol{e}_x + \bar{v}\boldsymbol{e}_y$), $g(z)$ is a parabolic function $g(z) = 3(1-z^2/d^2)/2$, $\bar{\boldsymbol{v}}_{ev}$ and $\bar{\boldsymbol{v}}_{eo}$ are the electroviscous and electro-osmotic velocity perturbation. Here, the overbar denotes a depth-averaged quantity. The electro-osmotic velocity perturbation is

$$\bar{\boldsymbol{v}}_{eo} = -u_0 \left(\left(\frac{\partial_x \bar{\phi}}{E_a} + n \frac{\bar{\sigma}}{\sigma_0} \right) \boldsymbol{e}_x + \left(\frac{\partial_y \bar{\phi}}{E_a} \right) \boldsymbol{e}_y \right), \tag{4.14}$$

where E_a is the applied electric field which is assumed to be uniform. The z-dependence of velocity perturbation disappears after depth-averaging,

$$\rho \frac{\partial \bar{\boldsymbol{v}}}{\partial t} + \rho(\boldsymbol{v}_0 \cdot \nabla_H)\bar{\boldsymbol{v}} + \rho(\bar{\boldsymbol{v}} \cdot \nabla_H)\boldsymbol{v}_0 = -\nabla_H \bar{p} + \mu \nabla_H^2 \bar{\boldsymbol{v}} - \frac{3\mu}{d^2}(\bar{\boldsymbol{v}} - \bar{\boldsymbol{v}}_{eo}) + \bar{\rho}_f \boldsymbol{E}_0, \tag{4.15}$$

where $\boldsymbol{E}_0 = E_a \boldsymbol{e}_x$. The form of other governing equations (4.1*a*)–(4.1*c*) essentially remains unchanged, see Appendix A for details.

The viscous damping is mainly due to the walls at $z = \pm d$ because the thin-depth length scale d is much smaller than the horizontal length scale h. The Hele-Shaw-type electroviscous velocity profile, (4.13), is justified because momentum rapidly diffuses across the narrow channel depth. The viscous diffusion time scale is $\tau_v = d^2/\nu \simeq 3 \times 10^{-5}$ s for the experimental conditions in this paper where ν is kinematic viscosity, while the time scale of interest is usually larger than 0.1 s in this paper.

4.4. *Scaling analysis*

The following scaling is adopted,

$$x, y \sim h, \quad u_0 \sim U_{eo}, \quad t \sim h/U_{eo}, \quad \sigma_0 \sim \sigma_r, \tag{4.16a}$$

$$\bar{u}, \bar{v} \sim U_{ev}, \quad \bar{p} \sim \mu U_{ev} h/d^2, \quad \bar{\phi} \sim E_a h, \quad \bar{\sigma} \sim \sigma_r, \tag{4.16b}$$

where the bars denote depth-averaged perturbation. It is important to note that U_{eo} is the velocity scale for base electro-osmotic flow and is used to scale time. On the

other hand, U_{ev} is the internally generated velocity scale used to non-dimensionalize the perturbation velocity. Since charge density has already been properly scaled to account for conductivity gradients (see (4.10)), both base and perturbed conductivities are scaled with σ_r for simplicity.

The linearized governing equations can be reduced to the non-dimensional form as presented in Appendix A (see (A14)). The conservation of conductivity and x-momentum equations are restated here,

$$\varepsilon^{-1}Pe(\partial_T \bar{\Sigma} + U_0\partial_X \bar{\Sigma} + R_v(\partial_Y \Sigma_0)\bar{V}) = \nabla_H^2 \bar{\Sigma}, \tag{4.17}$$

$$\varepsilon Re(\partial_T \bar{U} + U_0\partial_X \bar{U} + (\partial_Y U_0)\bar{V}) = -\partial_X \bar{P} + \varepsilon^2 \nabla_H^2 \bar{U} - 3(\bar{U} - \bar{U}_{eo}) - \Gamma^{-1} L_d \nabla_H^2 \bar{\Phi}, \tag{4.18}$$

where $L_d = \delta/h$ is the nondimensional diffusion length. Capital letters denote non-dimensional variables (except E which does not appear in the non-dimensional equations), and a general field variable Q is decomposed in non-dimensional form as $Q = Q_0 + \bar{Q}$. An electroviscous-to-electro-osmotic velocity ratio R_v is defined as

$$R_v = \frac{U_{ev}}{U_{eo}} = \Gamma \frac{E_a d^2}{\zeta_r \delta}. \tag{4.19}$$

An electric Rayleigh number Ra_e is defined as

$$Ra_e = \varepsilon^{-1} Pe\, R_v = \frac{U_{ev} h}{D_{eff}} = \Gamma \frac{h}{\delta} \frac{\epsilon E_a^2 d^2}{\mu D_{eff}}, \tag{4.20}$$

which measures the relative importance of dynamic (electric body) forces to dissipative forces due to molecular and viscous diffusion. It will be shown below that Ra_e controls the onset of instability and R_v controls the onset of absolute instability. For a given system, both the velocity ratio and Rayleigh number vary with electric field and are not independent of each other,

$$\frac{Ra_e}{R_v^2} = \frac{1}{\Gamma} \frac{h\delta}{d^2} \frac{\epsilon \zeta_r^2}{\mu D_{eff}} = \Upsilon \frac{Z_r^2}{\varepsilon^2}, \tag{4.21}$$

where $\Upsilon = L_d/\Gamma$ accounts for the effects of diffusive conductivity profile, and the reference zeta potential ζ_r is non-dimensionalized as,

$$Z_r = \frac{\zeta_r}{\sqrt{\mu D_{eff}/\epsilon}}. \tag{4.22}$$

The reduced zeta potential Z_r is a measure of the convection ability of electro-osmotic flow against dissipative forces in the system.

5. Linear stability analysis

This section outlines the procedures and algorithms for linear stability analysis. First of all, the linearized governing equations are recast in a matrix form,

$$\partial_X \boldsymbol{\xi} = \mathscr{A}\boldsymbol{\xi} + \mathscr{B}\partial_T \boldsymbol{\xi}, \tag{5.1}$$

where,

$$\boldsymbol{\xi} = (\bar{\Sigma}, \partial_X \bar{\Sigma}, \partial_X \bar{\Phi}, \partial_Y \bar{\Phi}, \bar{U}, \bar{V}, \partial_X \bar{V}, \bar{P})^T. \tag{5.2}$$

The specific forms of matrix operators $\mathscr{A}$ and $\mathscr{B}$ together with the base state and boundary conditions are discussed in Appendix B.

5.1. *Eigenvalue solution for convective instability*

We first discuss the eigenvalue solution to the set of governing equations in a spatial framework. This approach is particulary relevant in the case of convective instability. Assuming temporally periodic perturbation,

$$\bar{\boldsymbol{\xi}}(X, Y, T) = \hat{\boldsymbol{\xi}}(X, Y)\mathrm{e}^{-\mathrm{i}\Omega T}, \tag{5.3}$$

where Ω is the non-dimensional radian frequency, the system of equations can be recast as an eigenvalue problem,

$$\partial_X \hat{\boldsymbol{\xi}} = (\mathscr{A} - \mathrm{i}\Omega\mathscr{B})\hat{\boldsymbol{\xi}}. \tag{5.4}$$

In the spatial framework, spatially amplifying eigenmodes are sought for a given (real) frequency. The possible eigenmodes are given by

$$\bar{\boldsymbol{\xi}} = \hat{\boldsymbol{\xi}}_e(Y)\,\mathrm{e}^{\mathrm{i}(K_e X - \Omega T)}, \tag{5.5}$$

where K is the non-dimensional wavenumber, subscript e denotes eigenvalue solution, and $\hat{\boldsymbol{\xi}}_e(Y)$ is the eigenfunction corresponding to K_e.

5.2. *Eigenvalue solution for temporal stability*

If, on the other hand, an eigenvalue solution in a temporal framework is desired, a spatially periodic perturbation can be assumed of the form,

$$\bar{\boldsymbol{\xi}}(X, Y, T) = \check{\boldsymbol{\xi}}(Y, T)\,\mathrm{e}^{\mathrm{i}KX}. \tag{5.6}$$

The system of equations can then be recast as a generalized eigenvalue problem,

$$\mathscr{B}\partial_T \check{\boldsymbol{\xi}} = (-\mathscr{A} + \mathrm{i}K\mathscr{I})\check{\boldsymbol{\xi}}, \tag{5.7}$$

where $\mathscr{I}$ is the identity matrix. In the temporal framework, temporally amplifying eigenmodes are sought for a given (real) wavenumber. The possible eigenmodes are given by

$$\bar{\boldsymbol{\xi}} = \check{\boldsymbol{\xi}}_e(Y)\,\mathrm{e}^{\mathrm{i}(KX - \Omega_e T)}, \tag{5.8}$$

where $\check{\boldsymbol{\xi}}_e(Y)$ is the eigenfunction corresponding to Ω_e.

The advantage of this approach is that the same matrices $(\mathscr{A}, \mathscr{B})$ and therefore the same numerical code can be used for both spatial and temporal stability analysis. This is convenient as eigenvalue solutions of temporal instability are required for applying Briggs–Bers criteria as discussed below. Furthermore, because temporal and convective instability share the same onset condition for instability (Schmid & Henningson 2001), it is often advantageous to solve the temporal stability problem in order to compute the marginal stability boundary efficiently.

5.3. *Numerical procedures*

Chebyshev collocation (Trefethen 2001) in the Y-direction is used throughout this paper. The eigenvalues and eigenfunctions are computed using a built-in Matlab solver for generalized eigenvalue problems (MathWorks, Natick, MA, USA). With sixteen mesh segments ($N = 16$), the numerical scheme yields at least two-digit accuracy; $N = 32$ yields at least four-digit numerical accuracy.† Unless specified otherwise,

† For this particular problem, the convergence is typically slower for larger growth rates ($-K_i$). For the parametric space reported in this paper, Chebyshev collocation with $N = 16$ is enough to yield numerical accuracy of two significant digits. For example, with the parameters presented

	Description	Value	Notes
d^*	half depth	5.5×10^{-6} m	Experimental measurement
h^*	half width	7.8×10^{-5} m	Experimental measurement
ρ^*	density	1.0×10^{3} kg m^{-3}	Property of pure water
μ^*	dynamic viscosity	1.0×10^{-3} kg m^{-1} s^{-1}	Property of pure water
ϵ^*	permittivity	6.9×10^{-10} C V^{-1} m^{-1}	Property of pure water
D^*_{eff}	effective diffusivity	1.0×10^{-9} m^2 s^{-1}	Definition (3.6) and measurement
γ^*	conductivity ratio	10	Experimental mesurement
δ^*	half diffusion length	1.9×10^{-5} m	Diffusion length assumed *uniform*
n^*	correlation coefficient	0	Zeta potential assumed *uniform*
ζ^*_r	reference zeta potential	1.4×10^{-2} V	*Modelling* result and measurement

TABLE 2. Parameters for linear stability analysis. Assumptions are highlighted by *italics*. Throughout the paper, asterisk (*) denotes approximations to experimental conditions with values presented in this table.

results using $N = 16$ are presented in this paper, and these results were spot-checked with $N = 32, 64$ to ensure numerical convergence. Finite-difference solutions with various meshes (including uniform, cosine and tanh) have also been used to validate the pseudospectral code.

The linear stability analysis is performed in the spatial framework as shown in § 5.1 unless otherwise specified. The spatial stability analysis is known to produce spurious roots, see for example Schmid & Henningson (2001). Although comparison between two different numerical methods can aid the elimination of spurious roots, we rely on the more rigorous Briggs' test as the major method used for selecting physical modes. Briggs–Bers criteria can be used to differentiate physically amplifying roots from spurious roots based on the principle of causality (Briggs 1964; Bers 1983). Using Briggs' test as a guide, the physical modes which are convectively unstable can be numerically tracked by continuation. Details of this procedure can be found in Appendix C.1.

6. Numerical results

In this section, we shall first investigate the instability dynamics using the set of parameters presented in table 2. The effects of diffusive conductivity profile and non-uniform electro-osmotic flow are investigated subsequently. Other parametric variations are presented in the next section.

Table 2 shows the parameters chosen to approximate experimental conditions. This set of parameters is denoted by an asterisk (*) and serves as a control case in the paper. The channel geometry was experimentally measured. The permittivity, viscosity and density of dilute borate solutions were taken to be those of pure water. The effective diffusivity D^*_{eff} was obtained from the diffusivities of Na^+ and $B(OH)^-_4$ ions according to its definition (3.6). The conductivity ratio was $\sigma^*_H/\sigma^*_L = 10$. The diffusion length was assumed to be uniformly 25% of the channel width, which is the diffusion length approximately one channel width downstream for the base state at 1.0 kV cm^{-1}.

in table 2 and at $Ra_e = 116$, $\Omega = 2.30$, the eigenvalue solution corresponds to a most unstable eigenmode with a medium growth rate. With increasing mesh refinement, the eigenvalues are: $N = 16$: $K = 2.30485 - 0.494031\,\mathrm{i}$; $N = 32$: $K = 2.29827 - 0.500228\,\mathrm{i}$; $N = 64$: $K = 2.29828 - 0.500233\,\mathrm{i}$.

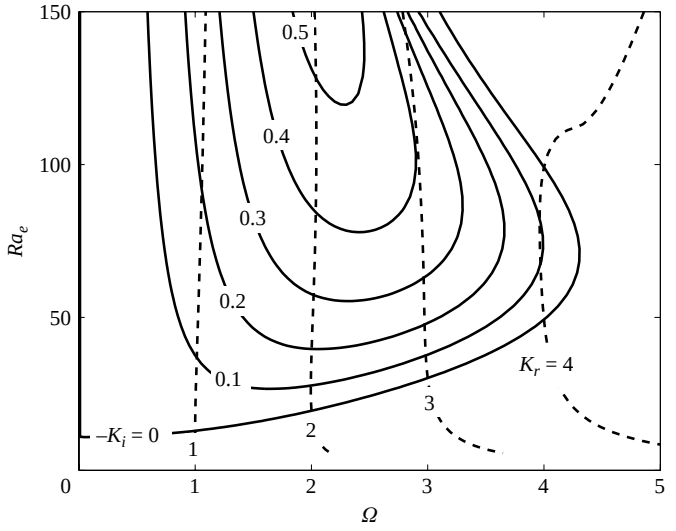

FIGURE 9. Convective instability: contours of spatial growth rate $-K_i$ (solid lines) and wave numbers K_r (dashed lines) as a function of temporal frequency Ω and electric Rayleigh number Ra_e. The parameters are described in table 2. The system is unstable for electric Rayleigh number above a threshold of $Ra_{e,cr} = 11$. Lines of constant wavenumbers are almost parallel to the vertical axis, i.e. to lines of constant frequency, indicating a constant phase speed which is equal to the reference electro-osmotic velocity.

Zeta potential was assumed to be uniform ($n^* = 0$). The reference zeta potential ζ_r^* (at the channel centreline where $\sigma_r^* = (\sigma_H^* + \sigma_L^*)/2$) was chosen as the value which best approximates the group velocity of initial disturbances for the uniform electro-osmotic flow case. For a pulse disturbance in the regime of convective instability, it has been proved that the maximum growth rate is observed by moving at a group velocity

$$v_g = \left(\frac{\partial \omega_r}{\partial k} \right)_{k_m}, \tag{6.1}$$

where ω_r is the real part of the temporal frequency corresponding to a wavenumber k, and k_m is the wavenumber of the most unstable mode in the temporal stability analysis (Briggs 1964, pp. 23–27). Using the method presented in § 5.2, this group velocity was calculated to be equal to the reference electro-osmotic velocity in the uniform electro-osmotic flow case, provided that the conditions are reasonably below the absolute instability threshold.† Experimentally, this group velocity was measured by tracking the wavefront ('valley') of the initial disturbance as described in § 2.2. Comparing experimental and numerical results, a reference zeta potential of 14 mV was obtained.

6.1. *Convective and absolute instability*

Figure 9 shows contours of the spatial growth rates and wavenumbers in the regime of convective instability. There is a threshold for the onset of convective instability

† For the case presented in table 2, if $E_a < 0.52\,\mathrm{kV\,cm^{-1}}$ ($Ra_e < 150$, $R_v < 3.9$), the group velocity is equal to the reference electro-osmotic velocity ($v_g = U_{eo}$) for the most unstable temporal modes. These limits are to be compared with the onset conditions of absolute instability: $E_{a,cr} = 0.65\,\mathrm{kV\,cm^{-1}}$ ($Ra_e = 240$, $R_v = 4.9$).

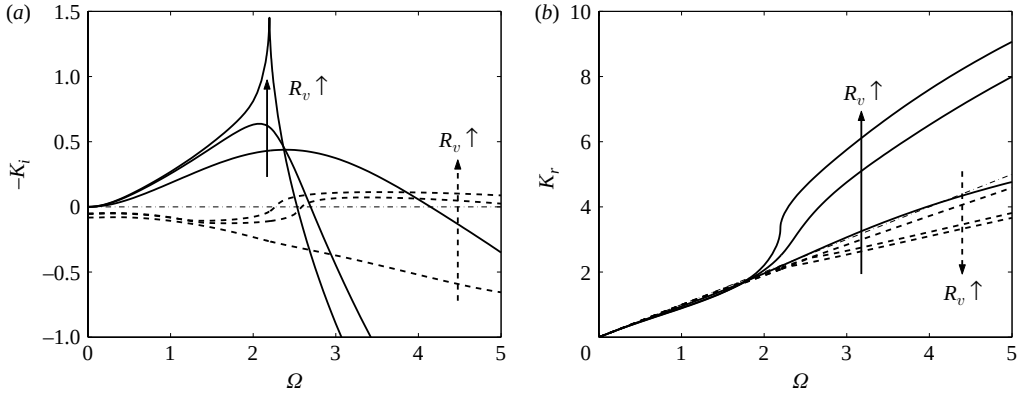

FIGURE 10. Absolute instability: detection by cusp point in the spatial growth rate ($-K_i$) *vs.* temporal frequency (Ω) curve. The solid and dashed curves are for two distinct unstable eigenmodes, respectively, and velocity ratios are $R_v = 3.0, 4.5, 4.9$ ($Ra_e = 90, 200, 240$) with arrow denoting increasing direction. Other parameters are described in table 2. (*a*) Spatial growth rate as a function of frequency: a cusp point is evident at $R_v = 4.9$ for the absolutely unstable mode (solid lines). (*b*) Wavenumber (K_r) as a function of frequency: for the absolutely unstable mode, wave speed is equal to electro-osmotic velocity (along the dot-dashed line) for low R_v, but decreases as R_v increases, e.g. at $\Omega = 3$.

at $Ra_{e,cr} = 11$. Above this threshold, the system is unstable for long waves at low electric Rayleigh number. For a Rayleigh number above 50, the most unstable modes have nearly constant wavelengths. The constant-wavenumber lines nearly coincide with constant-frequency lines (particulary for $K_r = 1, 2$), which means phase speed ($V_{ph} = \Omega/K_r$) is constant for low-frequency waves, and, more importantly, for the most unstable waves. This phase speed is equal to the reference electro-osmotic velocity U_{eo}. The non-dimensional spatial growth rate is of order unity.

Figure 10(*a*) shows the onset of absolute instability as indicated by a cusp point in the spatial growth rate ($-K_i$) versus temporal frequency (Ω) curve with increasing velocity ratios. At low R_v, phase speed is constant and equal to electro-osmotic velocity. At higher R_v, phase speed decreases at $\Omega > 2$ (figure 10*b*), and a cusp point appears at $\Omega = 2.2$ for $R_v = 4.9$ in the growth rate versus frequency plot (figure 10*a*). This cusp point corresponds to a zero group velocity ($\partial\Omega/\partial K$), and is an indication of a possible absolute instability (Huerre & Monkewitz 1985; Huerre & Rossi 1998). As shown in Appendix C.2, Briggs–Bers criteria can be employed to demonstrate that this cusp point indeed corresponds to an absolute instability. Note that two distinct modes can become unstable, one mode (denoted by solid lines) can become absolutely unstable, the other (dashed lines) can only become convectively unstable.

6.2. *Influence of diffusive conductivity profile*

Figure 11 shows the influence of increased diffusion length. The qualitative features of convective and absolute instability remain unchanged. For example, the most unstable waves still have a phase speed equal to the electro-osmotic velocity. The most notable difference is that the frequency for most unstable waves decreases, e.g. the onset of absolute instability is at $\Omega = 1.4$ compared to 2.2 for the control case, and the range of frequencies for unstable waves decreases. Similar effects were observed if conductivity ratio was decreased.

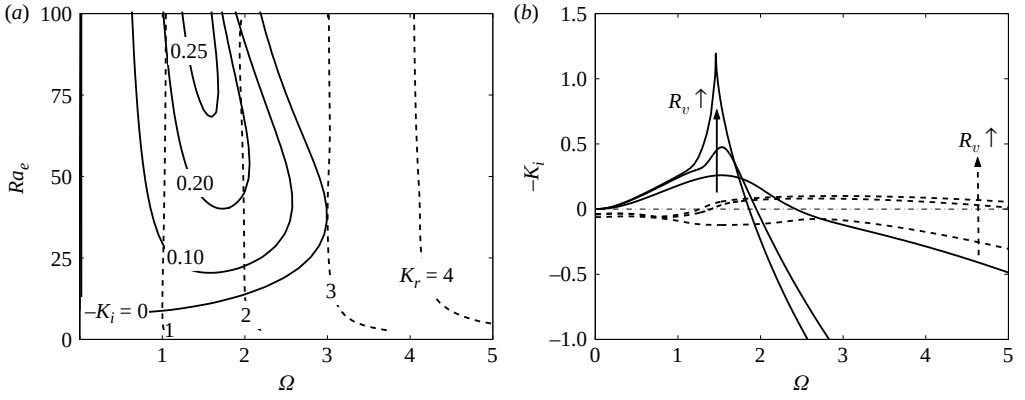

FIGURE 11. Effects of diffusion length. Diffusion length $\delta = 2\delta^*$ ($L_d = 0.5$), other parameters are described in table 2. (*a*) Convective instability occurs at $Ra_{e,cr} = 7.8$, the most unstable modes shift to a lower frequency compared to the control case. (*b*) Absolute instability occurs at $R_{v,cr} = 3.2$. The three velocity ratios are $R_v = 2.0, 3.0, 3.2$ ($Ra_e = 80, 180, 210$).

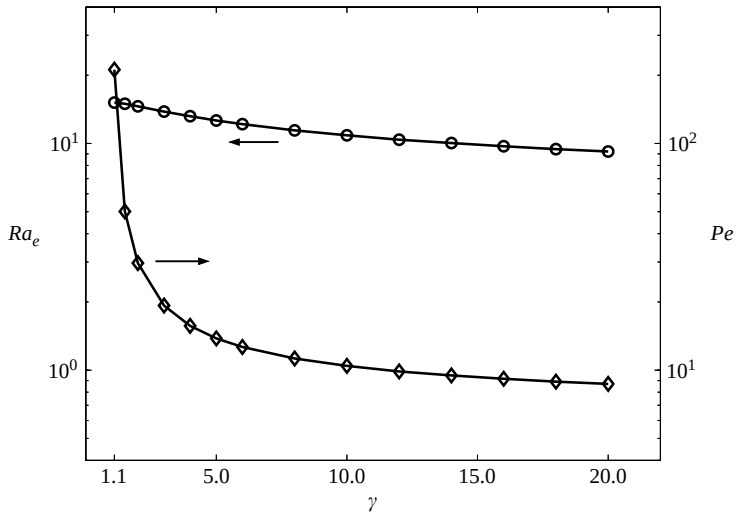

FIGURE 12. Onset of convective instability: critical electric Rayleigh number ($Ra_{e,cr}$). Conductivity ratios (γ) are varied, other parameter are described in table 2. Rayleigh number (○) and Péclet number (◇) are plotted for γ varying from 1.1 to 20. The onset conditions occur at approximately $Ra_{e,cr} \simeq 10$.

Figure 12 shows the effects of various conductivity ratios. The onset conditions for convective instability are plotted. Although the Péclet number for the onset of convective instability changes by more than an order of magnitude for conductivity ratios ranging from 1.1 to 20, the onset conditions for convective instability all have a critical Rayleigh number of approximately $Ra_{e,cr} \simeq 10$. This observation leads to and supports further discussion in the next section on Ra_e controlling the onset of convective instability.

6.3. *Influence of non-uniform electro-osmotic flow*

So far we have treated electro-osmotic flow as uniform. Zeta potential usually has a dependence on ionic concentration, which is proportional to conductivity. As discussed

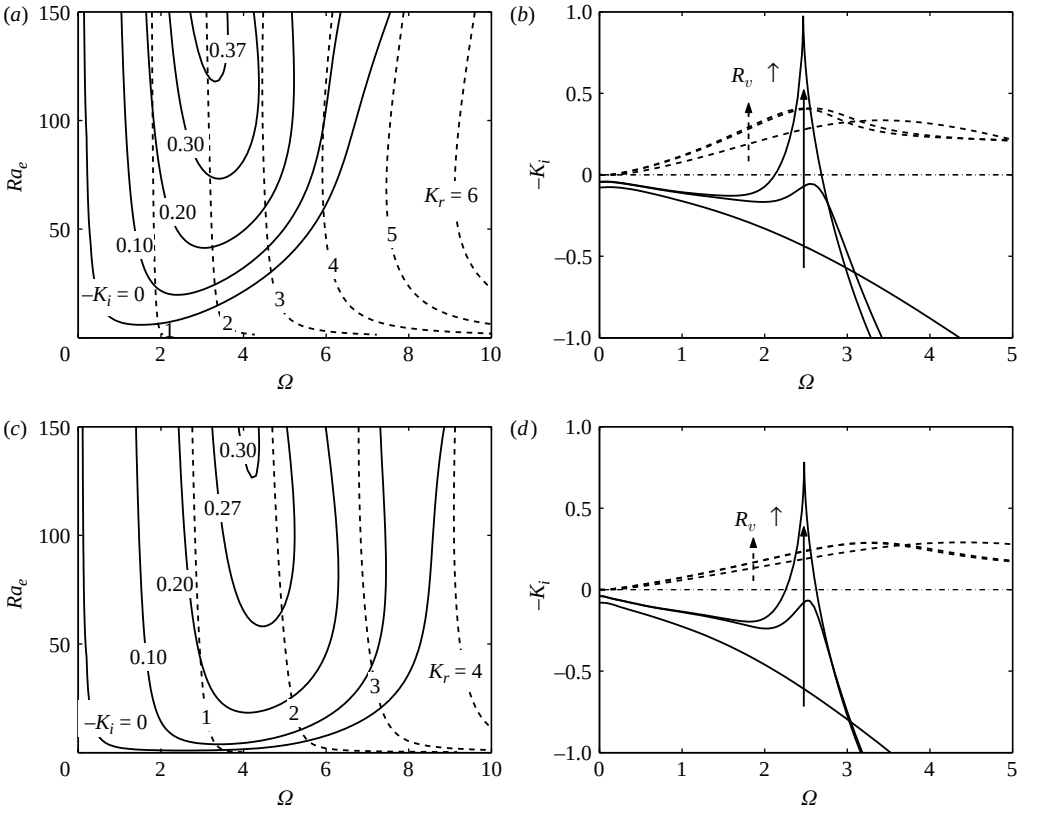

FIGURE 13. Effects of zeta dependence on conductivity. Correlation coefficients are: (a, b) $n = 1/4$; (c, d) $n = 1/2$. (a, c) Convective instability, (b, d) appearance of absolute instability. The velocity ratios are: (b) $R_v = 3.0, 5.2, 5.5$ $(Ra_e = 90, 270, 300)$; (d) $R_v = 3.0, 6.0, 6.2$ $(Ra_e = 90, 360, 380)$. Other parameter are described in table 2. Both cases suggest that the qualitative features of instability dynamics remain unchanged compared to the uniform electro-osmotic flow $(n = 0)$ case.

in § 4.1, we shall use two power laws coefficients $(n = 1/4, 1/2)$ to investigate the effects of electro-osmotic flow on the instability dynamics. In addition, the magnitude of zeta potential is varied to establish the convective role of electro-osmotic flow.

Figure 13 shows the effect on the stability dynamics by including a dependence of zeta potential on conductivity. Three differences with respect to the control case are worth noting. First, the onset of convective instability is now at a non-zero frequency (figure 13*a*, *c vs.* figure 9), and the waves at onset are no longer in the long-wave limit. Hence, the double-layer response to bulk conductivity (and its associated velocity gradients) can act as a stabilizing mechanism. Secondly, the magnitude of phase speed increases for both cases, $V_{ph} \simeq 1.5U_{eo}$ for $n = 1/4$ and $V_{ph} \simeq 2.5U_{eo}$ for $n = 1/2$. This increase in phase speed is partially due to our particular non-dimensionalization: the average zeta potential is higher than the zeta potential at the centreline because of the nonlinear power law. Last, the absolutely and convectively unstable modes change order along the growth rate axis, i.e. at $\Omega = 0$ (figure 13*b*, *d vs.* figure 10*a*): the absolutely unstable mode starts below the origin in figure 13, but starts from the origin for the control case in figure 10. Similar phenomena were observed for low-conductivity-ratio cases. Because of this solution behaviour, it is important to

	$n=0$					$n=1/4$					$n=1/2$				
	Ra_e	R_v	Ω	K_r	$-K_i$	Ra_e	R_v	Ω	K_r	$-K_i$	Ra_e	R_v	Ω	K_r	$-K_i$
Conv/Crit	11	1.0	0	0	0	5.9	0.77	1.5	0.74	0	0.92	0.30	2.5	0.65	0
Abs/Crit	240	4.9	2.2	3.3	1.5	300	5.5	2.5	4.0	1.0	380	6.2	2.5	4.7	0.82
$\zeta_r=\zeta_r^*$	140	3.7	2.2	2.2	0.54	140	3.7	3.2	2.1	0.39	140	3.7	4.2	1.7	0.30
$\zeta_r=5\zeta_r^*$	140	0.75	2.1	2.1	0.094	140	0.75	2.2	1.4	0.097	140	0.75	2.7	1.1	0.099
$\zeta_r=10\zeta_r^*$	140	0.37	2.1	2.1	0.047	140	0.37	1.8	1.2	0.063	140	0.37	2.1	0.89	0.062

TABLE 3. Effects of electro-osmotic flow: zeta dependence on conductivity and magnitude of zeta potential. The top row is the condition at onset of convective instability, and second row is at onset of absolute instability. Frequency Ω, wave number K_r and growth rate $-K_i$ correspond to the most unstable eigenmodes. The three bottom rows are the most unstable modes at a fixed electric Rayleigh number with three different magnitudes of zeta potential.

inspect all the modes in the eigenspectrum instead of tracking one particular mode, and Briggs–Bers criteria are excellent tools for this purpose (see Appendix C for details).

Despite these notable differences, the essential instability dynamics for various power law coefficients (e.g. $n=1/4, 1/2$) remain the same as in the control case ($n=0$). For example, the system becomes convectively and absolutely unstable above certain thresholds, and the most unstable wave length and wave speed are constant for waves with reasonable growth rates (>0.2). As shown in table 3, the critical conditions for convective and absolute instabilities are similar. For a medium Rayleigh number between convective and absolute instability, the frequency, wavenumber and growth rates for all three power laws are within a factor of two.

Table 3 also shows the influence of the magnitude of zeta potential. For the uniform electro-osmotic flow case, the frequency and wavenumber remain unchanged for increasing zeta potential, but the growth rate decreases nearly linearly. This suggests that the major role of electro-osmotic flow is to convect the disturbance downstream – a high convection velocity gives the unstable waves less time to grow before they reach a certain downstream location. For non-uniform electro-osmotic flow with $n=1/4, 1/2$, the growth rate decreases with zeta potential although to a somewhat lesser degree. Again, the quantitative stability characteristics are within a factor of two.

The results above suggest that the overall qualitative dynamics remain unchanged for different power laws of zeta dependence on conductivity. The quantitative features are usually within a factor of two for various power laws. Therefore, we shall concentrate on the uniform electro-osmotic flow case ($n=0$) in order to reveal the essential physics of the instability.

In order to confirm the observation of electro-osmotic flow as a carrying medium, zeta potential is varied over one order of magnitude for the uniform electro-osmotic flow case and the resulting onset condition for absolute instability is plotted in figure 14. While Rayleigh number changes by two orders of magnitude, the critical velocity ratio remains nearly constant. In particular, when $Z_r \geqslant 1$, the critical velocity ratio is nearly constant at $R_{v,cr}=3.7$.† As discussed above (see (4.22)), the reduced

† As $Z_r \to 0$, the critical condition for onset of absolute instability $R_v \to \infty$. This is because when electro-osmotic flow is negligible, the onset of absolute instability coincides with that of the convective instability, so the critical electric field is still finite as Z_r approaches zero. Of course, this limit is not of interest to the electrokinetic instability study in this paper.

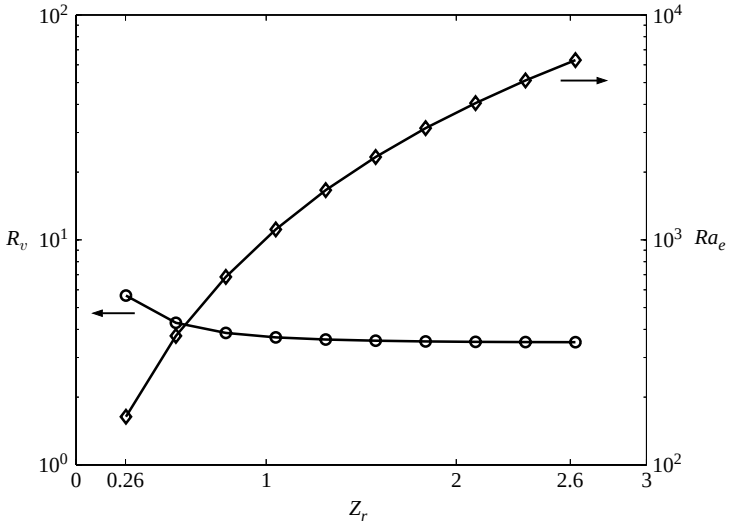

FIGURE 14. Onset of absolute instability: critical velocity ratio ($R_{v,cr}$). The non-dimensional zeta potential (Z_r) is varied from 0.26 to 2.6 ($\zeta_r = 10$–$100\,\mathrm{mV}$), other parameters are described in table 2. Electroviscous-to-electro-osmotic velocity ratio (○) and electric Rayleigh number (◇) are plotted. The onset conditions occur at approximately $R_{v,cr} \simeq 4$.

zeta potential Z_r is a measure of the convection ability of electro-osmotic flow. When Z_r is above unity, increasing zeta potential only increases the speed of convection and decreases the spatial growth rate correspondingly. This explains the linear decrease of growth rate from $\zeta_r = 5\zeta^*$ to $10\zeta^*$ in table 3.

7. Physics of instability

In this section, we will first derive an analytical solution to the electrohydrodynamic instability with no electro-osmotic flow. When electro-osmotic flow is present, a transformation from temporal to spatial framework contributes to the understanding of the electrokinetic instability mechanism. The physical insight then serves as guidelines to a systematic parametric variation.

7.1. *Analytical solution without electro-osmotic flow*

In order to unfold the instability mechanism, let us examine the simplest case in the thin-depth limit ($\varepsilon \to 0$) with no electro-osmotic flow ($\zeta_r = 0$). Because there is no electro-osmotic flow, time has to be re-scaled. The natural choice is the intrinsic time scale h/U_{ev}, and the new non-dimensional time is denoted by $\tilde{T}$. This linear stability problem can be solved in the temporal framework by assuming spatial periodicity in X.

In the thin-depth limit with no electro-osmotic flow, the linearized governing equations (A14) are simplified to,

$$Ra_e(\partial_{\tilde{T}}\bar{\Sigma} + (\partial_Y \Sigma_0)\bar{V}) = \partial_X^2\bar{\Sigma} + \partial_Y^2\bar{\Sigma}, \tag{7.1a}$$

$$\Sigma_0^{-1}(\partial_X\bar{\Sigma} - (\partial_Y \Sigma_0)\partial_Y\bar{\Phi}) = \partial_X^2\bar{\Phi} + \partial_Y^2\bar{\Phi}, \tag{7.1b}$$

$$\partial_X\bar{U} + \partial_Y\bar{V} = 0, \tag{7.1c}$$

$$\partial_X \bar{P} + 3\bar{U} + \Upsilon\left(\partial_X^2 \bar{\Phi} + \partial_Y^2 \bar{\Phi}\right) = 0, \tag{7.1d}$$

$$\partial_Y \bar{P} + 3\bar{V} = 0, \tag{7.1e}$$

where $Ra_e = U_{ev}h/D_{eff}$ remains the same (see (4.20)). Note that the inertial terms and horizontal viscous terms in the momentum equations (7.1*d*)–(7.1*e*) are neglected for simplicity.

The Navier–Stokes equations (7.1*c*)–(7.1*e*) resemble that of the Hele-Shaw flow, except that a driving electric body force is added. By applying (7.1*c*), ∂_X (7.1*d*) + ∂_Y (7.1*e*) yields,

$$\nabla_H^2(\bar{P} + \Upsilon \partial_X \bar{\Phi}) = 0, \tag{7.2}$$

where $\nabla_H^2 = \partial_X^2 + \partial_Y^2$. Because $\bar{\Phi}$ and $\bar{P}$ are both periodic in X in the temporal stability analysis, and satisfy homogenous Neumann boundary conditions in Y ((B7*b*), and (B8*d*) as $\varepsilon \to 0$), the solution to the Laplace equation (7.2) is trivial,

$$\bar{P} = -\Upsilon \partial_X \bar{\Phi}. \tag{7.3}$$

Substituting (7.3) into (7.1*d*)–(7.1*e*),

$$\bar{V} = (\Upsilon/3)\partial_Y \partial_X \bar{\Phi}. \tag{7.4}$$

The two-dimensional velocity perturbation can also be expressed using a streamfunction

$$\bar{\Psi} = (\Upsilon/3)\partial_Y \bar{\Phi}, \tag{7.5}$$

where the streamfunction $\bar{\Psi}$ is defined such that $\bar{V} = \partial_X \bar{\Psi}$ and $\bar{U} = -\partial_Y \bar{\Psi}$.

Physically, equation (7.4) implies that any perturbation to the base electric field leads directly to a perturbation of the velocity field as stipulated by the Navier–Stoke equations. The stability of this dynamics, however, is coupled to the electro-diffusion of ions which is governed by the electrolytic Ohmic model, (7.1*a*)–(7.1*b*).

Using the explicit velocity-potential relation (7.4), (7.1*a*) and (7.1*b*) are a closed set of equations, which can be further reduced to a single equation in $\bar{\Phi}$ describing the instability dynamics,

$$\left(Ra_e \partial_{\tilde{T}} - \partial_X^2 - \partial_Y^2\right)\left((\partial_Y \ln \Sigma_0)\partial_Y + \partial_X^2 + \partial_Y^2\right)\bar{\Phi} = -(Ra_e \Upsilon/3)(\partial_Y \ln \Sigma_0)\partial_Y \partial_X^2 \bar{\Phi}. \tag{7.6}$$

The non-dimensionalization has been performed such that Ra_e takes into account the effects of diffusive conductivity profile. Although the quantitative features can still depend on specific profile (Σ_0 and Υ) as shown by (7.6), the dependence is much milder compared to the dependence on Ra_e (when proper scaling is used). Hence, the qualitative dynamics such as the onset condition is governed by the electric Rayleigh number. This argument is supported by the results of parametric variations presented at the end of this section.

Non-dimensional parameters similar to the electric Rayleigh number defined in (4.20) have been applied in other studies. For example, Baygents & Baldessari (1998) proposed a similar electric Rayleigh number which controls the onset of electrohydrodynamic instability in a system with linear conductivity gradient. Bruinsma & Alexander (1990) proposed the so-called Levich number which controls the onset of instability in electrolytic cells. Although these controlling parameters for electrohydrodynamic instability (including our electric Rayleigh number) are tailored to specific systems, they are all essentially the ratio of destabilizing electrical stresses to stabilizing dissipative stresses.

The instability mechanism is schematically presented in figure 15. When the initially flat interface is perturbed, the perturbed conductivity field will alter the electric field.

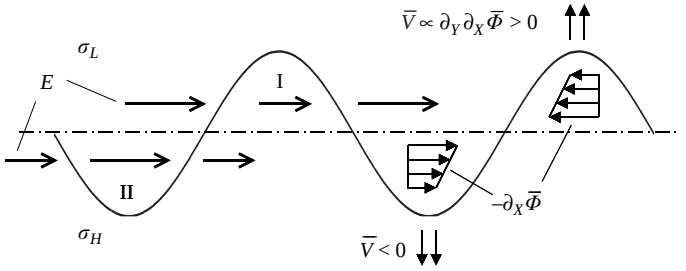

FIGURE 15. Schematic of electrohydrodynamic instability mechanism. When the conductivity interface is perturbed, the electric field is perturbed owing to alternation of conductivity. The perturbed electric field is strongest at the conductivity interface (dot-dashed line) and decays away from it, this gradient in electric field results in vertical velocities which further stretch the interface.

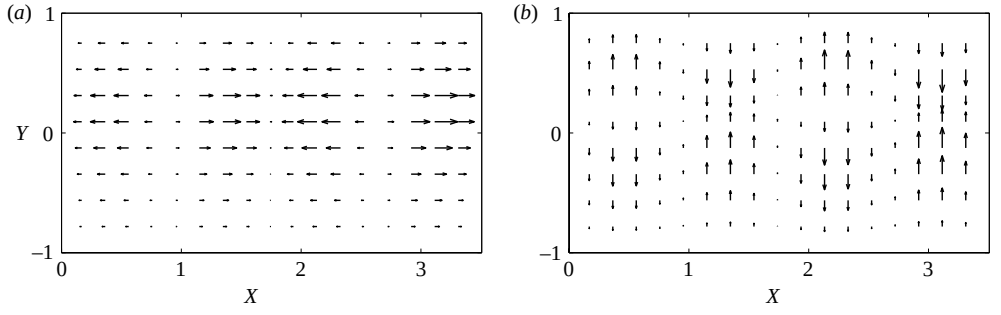

FIGURE 16. Eigenfunctions confirming velocity-potential relationship. (*a*) $\partial_X \bar{\Phi}$, negative electric field perturbation; (*b*) $\bar{V}$, y-component velocity perturbation. The relationship $\bar{V} \propto \partial_Y \partial_X \bar{\Phi}$ explains the correspondence between magnitudes of $\partial_X \bar{\Phi}$ and $\bar{V}$, see also figure 15. Numerical parameters: $Ra_e = 116$, $\Omega = 3.50$, others are described in table 2; mesh $N = 32$; eigenvalue $K = 3.58 - 0.144\,\mathrm{i}$.

The local electric field is strengthened where lower conductivity replaces higher conductivity (region II), and vice versa (region I). The electric field perturbation is strongest at the conductivity interface (dot-dashed line) and decays away from it. According to equation (7.4), the velocity perturbation further stretches the interface upward for regions I and downward for regions II. This tendency for the perturbed interface to be further stretched is competing with molecular diffusion. When Ra_e exceeds a critical value, the perturbation at the interface will grow and lead to instability.

7.2. *Mechanism of electrokinetic instability*

With the insight gained from the above asymptotic temporal instability analysis, we can now interpret the physical mechanism in the spatial framework. A uniform electro-osmotic flow does not change the fundamental stability characteristics. Although the actual electro-osmotic flow can be non-uniform, the numerical results in § 6.3 show that the major physics remain unchanged for such systems. For simplicity, therefore, we shall keep our discussion to the uniform flow case.

Figure 16 shows a typical eigenfunction solution. The numerical solution confirms the explicit velocity–potential relation (7.4) derived in the simplified asymptotic limit. It is worth noting that the actual conductivity interface is not sinusoidal but cellular

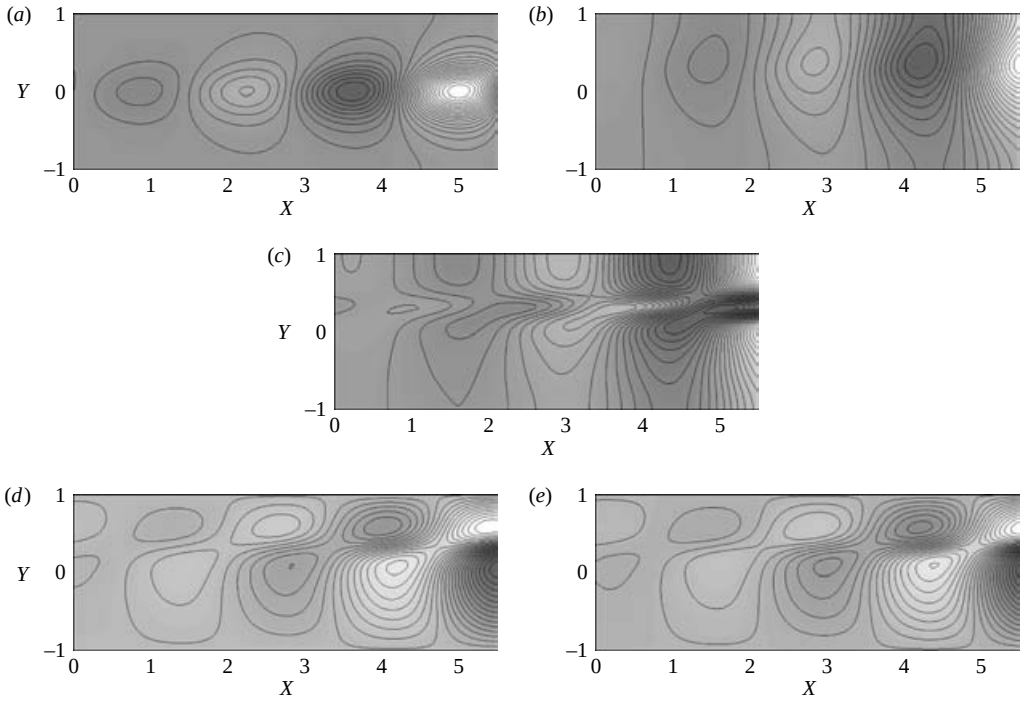

FIGURE 17. Electrokinetic instability mechanism shown by the most unstable eigenmodes. Dark grey is negative and light grey is positive, contour plots are overlayed: (*a*) $\bar{\Sigma}$, conductivity perturbation; (*b*) $\bar{\Phi}$, potential perturbation; (*c*) $\nabla_H^2\bar{\Phi}$, which is proportional to negative charge density; (*d*) $\bar{\Psi}$, streamfunction perturbation; (*e*) $\partial_Y\bar{\Phi}$, which approximates the streamfunction $\bar{\Psi}$ by equation (7.5). Conductivity perturbation alternates electric potential distribution and induces bulk charge accumulation, which in turn results in electric body forces and promotes cellular fluid motion. The cellular flow further perturbs the conductivity field and this positive feedback leads to instability. Numerical parameters: $Ra_e = 116$, $\Omega = 2.30$ ($E_a = 0.456\,\mathrm{kV\,cm^{-1}}$, $f = 2.08\,\mathrm{Hz}$), others are described in table 2; mesh $N = 32$; eigenvalue $K = 2.30 - 0.500\,\mathrm{i}$.

(as shown below), therefore the velocity profile in figure 16 does not exactly match the schematic in figure 15.

Figure 17 shows the most unstable eigenmodes. Figure 17(*a*): the eigenmode of conductivity perturbation has a cellular pattern and alternates in sign in the x-direction. Figure 17(*b*): such conductivity perturbation will change the electric potential distribution due to current continuity (equation (4.1*b*)). Figure 17(*c*): the perturbed electric field will produce a charge density perturbation by Gauss' Law (3.12), and leads to electric body forces. Figure 17(*d*): the electric body forces produce cellular fluid motion through Navier–Stokes equations (4.1*c*)–(4.1*d*). This fluid motion further alters the conductivity field through the convection-diffusion equation of conductivity (4.1*a*), and this positive feedback leads to instability. Figure 17(*e*): the contour of negative electric field ($\partial_Y\bar{\Phi}$) resembles that of the streamline, confirming the analytical expression (7.5).

In the presence of electro-osmotic flow, the unstable perturbations grow as they are convected downstream, which leads to convective instability if the disturbance is not too strong. In the regime of convective instability, growth rate is finite at any downstream location and the regions upstream of the initial disturbance are largely unaffected. However, when the internal perturbation (electroviscous) velocity

exceeds the carrying electro-osmotic velocity, the flow can become absolutely unstable. Absolute instability sets in when the disturbances grow fast enough such that the electro-osmotic flow cannot carry them downstream in time. In the regime of absolute instability, therefore, the disturbance grows in time (t) at the origin and the upstream flow is perturbed.

As an interesting side note to the role of electro-osmotic flow, the physically unstable eigenvalues are always associated with the 2×2 upper-diagonal sub-matrix of the governing matrix ($\mathscr{A} - \mathrm{i}\Omega\mathscr{B}$), which comes from the conductivity conservation equation (see Appendix B). At conditions slightly above the onset of convective instability ($Ra_e \gtrsim Ra_{e,cr}$), this sub-matrix can be used to predict the approximate location of the physically unstable modes in the eigen-spectrum (see details of this procedure in Chen 2004).

An important comparison to this work is the temporal stability analysis of an electrohydrodynamic instability with zero base flow (Hoburg & Melcher 1976, 1977). The mechanism proposed by Hoburg & Melcher is qualitatively similar to that described in figure 17. In the Ohmic regime, electrokinetics differs from electrohydrodynamics mainly in the presence of electro-osmotic flow, which leads to the convective and absolute electrokinetic instabilities described here. Such electrohydrodynamic instabilities coupled with electro-osmotic flow have, to date, not been reported in the electrohydrodynamics literature.

7.3. Ra_e–R_v instability phase diagram

Guided by the physical insights from the electrokinetic instability mechanism, we now study the controlling parameters for the onset of convective and absolute instability through a systematic parametric variation. The onset condition for convective instability is the same as that for temporal instability of the same system (Gaster 1962; Schmid & Henningson 2001). Hence, the critical condition for convective instability is still controlled by the electric Rayleigh number Ra_e which is the ratio of dynamic forces to dissipative forces. The onset condition for absolute instability is specific to spatial instability. As discussed above, absolute instability results when the electro-viscous disturbances grow faster than the electro-osmotic convection time scale. Hence, the onset condition for absolute instability is controlled by the relative velocity ratio $R_v = U_{ev}/U_{eo}$.

There are seven non-dimensional parameters in the problem: n, ε, L_d, Γ, Re, Ra_e and R_v. As discussed in § 6.3, the dependence of zeta potential on conductivity does not change the qualitative instability dynamics; we shall assume uniform electro-osmotic flow ($n = 0$) for simplicity. The other six parameters are varied in table 4.

Table 4 shows the selected parametric variations against the control case presented in table 2. The onset conditions of convective and absolute instability are reported for each case. Cases 1–6 present the effects of length scales including diffusion length. The results show that geometrically similar systems have the same onset conditions. If L_d is kept constant while length scales are changed, $Ra_{e,cr}$ remains unchanged (e.g. Cases 2 and 3, 5 and 6). Cases 7–9 present the effects of conductivity ratio, the onset conditions change very little for a wide range of γ (see also figure 12), confirming the discussion that Ra_e controls the instability as in equation (7.6). Cases 10–15 present the effects of material properties. Case 10 shows that inertial effects are not important. Case 11 shows viscosity and diffusivity play similar role as far as the onset conditions are concerned. Case 12 shows that zeta potential variation does not change the onset of convective instability, but influences the onset of absolute instability. Cases 13–15 show that the critical condition for absolute instability is the same if the reduced zeta

Case	Parameters varied	$Ra_{e,cr}$	$R_{v,cr}$	Ra_e/R_v^2	Notes
*		11	4.9	10	Control case: see table 2
1	$d = d^*/3$	11	3.2	90	Length scales
2	$h = 3h^*, \delta = 3\delta^*$	11	3.2	90	1 and 2: geometrically similar
3	$d = 3d^*, h = 3h^*, \delta = 3\delta^*$	11	4.9	10	3 and *: geometrically similar
4	$\delta = 0.8\delta^*$	13	5.7	8.0	Diffusion length
5	$\delta = 2\delta^*$	7.8	3.2	20	5: see also figure 11
6	$h = h^*/2$	7.8	5.6	5.0	5–6: same $L_d \Rightarrow$ same $Ra_{e,cr}$
7	$\gamma = \gamma^*/5$	15	3.0	60	Conductivity ratio
8	$\gamma = \gamma^*/2$	13	4.8	15	7–9: see also figure 12
9	$\gamma = 5\gamma^*$	11	3.3	7.3	
10	$\rho = 10\rho^*$	11	4.9	10	Material properties
11	$\mu = \mu^*/10, D_{eff} = 10D^*_{eff}$	11	4.9	10	10–11: same onset as *
12	$\zeta_r = 10\zeta_r^*$	11	3.5	1000	12–13: see also figure 14
13	$\zeta_r = 3\zeta_r^*$	11	3.7	9.0	13–15: same $Z_r \Rightarrow$ same $R_{v,cr}$
14	$\epsilon = 9\epsilon^*$	11	3.7	9.0	
15	$\mu = \mu^*/3, D_{eff} = D^*_{eff}/3$	11	3.7	9.0	

TABLE 4. Parametric variations against the control case. The parameters of the control case (denoted by an asterisk) are presented in table 2. The critical Raleigh number Ra_e and velocity ratio R_v are given. Note that for a given condition, Ra_e/R_v^2 is a constant so the corresponding Ra_e for $R_{v,cr}$ can be calculated, and vice versa.*, see table 2.

potential Z_r is kept constant. Combined with the observation in figure 14 that $R_{v,cr}$ is constant for $Z_r \geqslant 1$, these results suggest that $\sqrt{\mu D_{eff}/\epsilon}$ is the proper scaling for zeta potential.

Figure 18 plots the critical conditions on a $Ra_e - R_v$ phase diagram for a wide range of parameters presented in table 4. It is obvious from the figure that the onset of convective instability collapses around $Ra_{e,cr} \simeq 10$, while the onset of absolute instability collapses around $R_{v,cr} \simeq 4$. When the system properties are fixed, the electric Rayleigh number and the electroviscous-to-electro-osmotic velocity ratio vary along a fixed curve $Ra_e \propto R_v^2$. As the electric field is increased, the system first becomes convectively unstable when the Rayleigh number exceeds $Ra_{e,cr}$, and then absolutely unstable when the velocity ratio exceeds $R_{v,cr}$.

It should be noted that the $Ra_e - R_v$ phase diagram can be used to bound spatial growth rates. The growth rate at $Ra_e = Ra_{e,cr}$ is zero, and the growth rate at $R_v = R_{v,cr}$ is around unity for the parametric space we have explored; the spatial growth rates in the convective instability regime are bounded by these two cases. More importantly, for a given Ra_e which largely determines the temporal growth rate, a system with larger R_v (e.g. smaller zeta potential, see § 6.3) will usually have larger spatial growth rate.

8. Comparison between theory and experiments

This section compares the modelling results with experimental data, discusses the assumptions in the model, and suggests future work.

For the 10 : 1 conductivity ratio presented here, the experimentally observable features of the instability waves include: critical electric field ($E_{a,cr}$), spatial growth rate ($-k_i$), wavelength ($2\pi/k_r$), temporal frequency ($f = \omega/2\pi$), phase speed ($v_{ph} = \omega/k_r$)

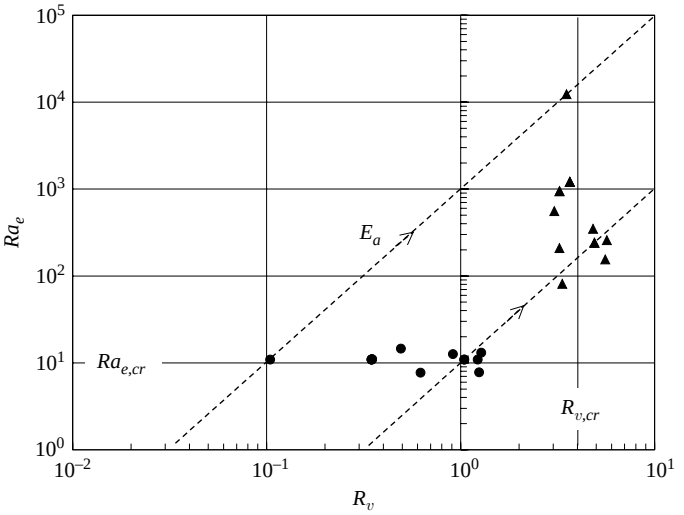

FIGURE 18. Phase diagram for convective and absolute instability. The critical conditions in table 4 are plotted, with circles representing the onset of convective instability, and triangles absolute instability. At a given condition, Ra_e/R_v^2 is a constant so Ra_e and R_v cannot be independently varied. As electric field is increased (in the direction of arrows), Ra_e and R_v for case 12 move along the upper dashed line ($Ra_e/R_v^2 = 1000$), while Ra_e and R_v for cases *, 3 and 10–11 move along the lower dashed line ($Ra_e/R_v^2 = 10$). At the onset of convective instability, the critical Rayleigh number collapses around $Ra_{e,cr} \simeq 10$. At the onset of absolute instability, the critical velocity ratio collapses around $R_{v,cr} \simeq 4$.

	Experiments	Theory
Convective instability $E_{a,cr}$	With threshold E-field of $(0.5 \pm 0.1)\,\mathrm{kV\,cm^{-1}}$	Controlled by Ra_e $0.14\,\mathrm{kV\,cm^{-1}}$
Absolute instability $E_{a,cr}$	Upstream perturbation observed at $1.5\,\mathrm{kV\,cm^{-1}}$	Controlled by R_v $0.65\,\mathrm{kV\,cm^{-1}}$
Spatial growth rate $-k_i$	Increases as E-field $(0.4 \pm 0.2)\ h^{-1}$ at $1.0\,\mathrm{kV\,cm^{-1}}$	Increases as E-field $0.54\ h^{-1}$ at $0.50\,\mathrm{kV\,cm^{-1}}$
Temporal frequency f	Increases as E-field (2.7 ± 1.2) Hz at $1.0\,\mathrm{kV\,cm^{-1}}$	Increases as E-field 2.2 Hz at $0.50\,\mathrm{kV\,cm^{-1}}$
Wavelength $2\pi/k_r$	Const for $0.75 - 1.25\,\mathrm{kV\,cm^{-1}}$ $(3 \pm 1)\ h$ at $1.0\,\mathrm{kV\,cm^{-1}}$	Const for $0.35 - 0.6\,\mathrm{kV\,cm^{-1}}$ $2.9\ h$ at $0.50\,\mathrm{kV\,cm^{-1}}$
Group velocity v_g	Linearly proportional to E $(0.93 \pm 0.1)\,\mathrm{mm\,s^{-1}}$ at $1.0\,\mathrm{kV\,cm^{-1}}$	Linearly proportional to E $\Rightarrow \zeta_r$ is set to 14 mV

TABLE 5. Comparison between experimental data and modelling results. Experimental electric field was applied voltage divided by a nominal length of 2 cm. Numerical results are reported for the most unstable eigenmode assuming uniform electro-osmotic flow.

and group velocity (v_g, see (6.1)). These quantities are summarized in table 5. This table shows a comparison of these experimental quantities (see § 2.2) with the results from linear stability analysis using the parameters presented in table 2.

The experimental measurements for these observable quantities are within a factor of three of the theoretical predictions. For example, the nominal threshold for onset of (convective) instability was $0.5 \pm 0.1\,\mathrm{kV\,cm^{-1}}$ in experiments, and is $0.14\,\mathrm{kV\,cm^{-1}}$ from

the linear stability analysis. The onset of absolute instability was about $1.5\,\mathrm{kV\,cm^{-1}}$ in experiments, and is $0.65\,\mathrm{kV\,cm^{-1}}$ from the analysis. The spatial growth rates estimated from experiments are also comparable to the model. In particular, the spatial growth rate was measured to be $1.1 \pm 0.4\,h^{-1}$ at $1.25\,\mathrm{kV\,cm^{-1}}$, an electric field close to the onset of absolute instability, this measurement is consistent with the numerical observation that the non-dimensional growth rate is around unity at the absolute instability threshold.

The model also captures a few trends of the instability waves with increasing electric fields, and these trends were indeed observed in the experiments. The model predicts that the wavelength is selected by the channel width ($2h$), and that temporal frequency is set by the electro-osmotic flow velocity ($f \propto U_{eo}/h$); therefore, the phase speed of the instability waves is proportional to electro-osmotic velocity. Results from temporal stability analysis also predict that the group velocity of a pulse disturbance is equal to electro-osmotic velocity (see discussion at the beginning of § 6). In experiments, the wavelengths were nearly constant (1–2 channel widths) for fields between $0.75 - 1.25\,\mathrm{kV\,cm^{-1}}$, and the temporal frequency increased with electric field in the convective regime. More importantly, the phase speed (which was proportional to the group velocity of initial disturbance) was a linear function of the applied electric field. This confirms the modelling insight that the main role of electro-osmotic flow is to carry the disturbances downstream in the regime of convective instability. When the disturbance is strong enough to overcome electro-osmotic flow, an absolute instability results and the upstream is perturbed. This theoretical prediction of absolute instability was observed at a field of $1.5\,\mathrm{kV\,cm^{-1}}$ in experiments.

In the instability wave analysis used in this comparison, we assumed a uniform diffusion length, and a uniform electro-osmotic flow. The constant zeta potential was empirically determined from the measured group velocity of the instability waves. The sensitivity to these parameters is discussed in §§ 6.2–6.3. Although non-uniform diffusion length is not discussed and the actual zeta-conductivity correlation is very difficult to determine in our experimental set-up, the current work suggests that these factors do not change the fundamental physics and do not significantly change the quantitative features either. The modelling results show that the most unstable wavelength increases with increasing diffusion length (figure 11), which is consistent with the experimental observation that wavelength increases downstream where diffusion length is also larger.

The thin-layer governing equations are asymptotically derived assuming the low-Rey-nolds-number ($\varepsilon Re \ll 1$) and low Péclet number ($\varepsilon Pe \ll 1$) limit. For the most unstable eigenmode at $0.46\,\mathrm{kV\,cm^{-1}}$, as described in figure 17, $\varepsilon = 7.1 \times 10^{-2}$, $Re = 2.4 \times 10^{-3}$, $Pe = 2.4$ and $R_v = 3.4$. Therefore, the low-Reynolds-number limit is easily satisfied, and $\varepsilon Pe = 0.17$ is sufficiently small for the purpose of our model. However, $\varepsilon Pe R_v = 0.58$ at $0.46\,\mathrm{kV\,cm^{-1}}$ and $\varepsilon Pe R_v = 1.2$ at $0.65\,\mathrm{kV\,cm^{-1}}$ (the onset of absolute instability). As a consequence, the low-Péclet-number limit is probably violated in the present experiments (see Appendix A, and particularly equation (A 2*a*)). It should be noted that if the sidewall effects (at $z = \pm d$) are not properly accounted for, a two-dimensional 'deep-water' linear stability analysis predicts a threshold electric field for convective instability which is an order of magnitude less than the thin-layer model (Chen *et al.* 2003). The fact that the thin-layer equations provide a critical electric field much closer to the experimental value is strong evidence for their usefulness as an approximation to our high-aspect-ratio experimental system. The utility of the thin-layer equations is also supported by the study of a similar electrokinetic instability in

a rectangular tube with a 10 : 1 aspect ratio, in which the strong damping effects of the sidewalls were demonstrated by comparing a two-dimensional 'deep-water' linear stability analysis with a linearized three-dimensional numerical simulation (Lin *et al.* 2004).

In future theoretical work, the Hele-Shaw type thin-layer equations deserve verification from a more complete numerical simulation. In addition, parabolized stability analysis (Schmid & Henningson 2001) would account for the non-parallel base state and may explain the dispersive nature of the instability waves better. In future experimental work, systematic parametric variations of length scales, conductivity profiles and material properties will help verify the scaling analysis and controlling parameters presented here. In order to test the theory of convective and absolute instability and confirm the role of electro-osmotic flow, controlled disturbances with known frequency and amplitude will be very useful. A geometrical design different from the perpendicular T-junction will clarify the role of the entrance region in the instability dynamics.

9. Conclusions

We have experimentally and analytically studied the electrokinetic instability in a high-aspect-ratio microfluidic T-junction with conductivity gradients. This instability has an experimentally observed threshold above which the flow is convectively unstable. At high electric field, upstream propagating waves were observed, indicating a possible absolute instability. Motivated by these experimental observations, we have developed an analytical model with numerical solutions which captures the salient physics of this instability. The governing equations (4.1) include the Navier–Stokes equations for fluid motion and an electrolytic Ohmic model with conservation equations for conductivity and current. In order to model the high-aspect-ratio experimental system, the thin-layer limit of these governing equations is adopted. The linear stability analysis shows results which capture the experimentally observed trends and compare very well with quantitative experimental data.

The instability mechanism is revealed through parametric variations guided by an analytical solution in the linearized thin-layer limit. Charge accumulation at interfaces of conductivity gradients leads to electric body forces which drive the coupled flow and electric field into an unstable dynamics. The scaling analysis, numerical results and comparison with experiments also illuminate the role of electro-osmotic flow in the instability. Electro-Osmotic flow convects disturbances downstream unless the internal electroviscous velocity perturbation is strong enough to overcome the bulk flow. This conclusion is supported by experimental results that clearly show a critical electric field for convective instability and indicate absolute instability at high fields. The role of electro-osmotic flow is also strongly supported by the two controlling parameters for the instability: Ra_e, the ratio of dynamic electric body forces to dissipative forces due to molecular and viscous diffusion, which controls the onset of instability; and R_v, the ratio of internally generated electroviscous velocity to bulk electro-osmotic velocity, which controls the convective versus absolute nature of instability.

This work was sponsored by DARPA (Contract Number F30602-00-2-0609) with Dr Anantha Krishnan as contract monitor and by an NSF CAREER Award (J. G. S.) with Dr Michael W. Plesniak as contract monitor. C. H. C. was funded by the William R. and Sara Hart Kimball Stanford Graduate Fellowship. We thank Mike Oddy, Jonathan Posner and Brian Storey for helpful discussions.

Appendix A. Asymptotic derivation of thin-layer governing equations

The thin-layer governing equations can be derived using asymptotic expansion as outlined in this Appendix. Figure 7 shows the schematic of the system of interest. We are interested in the thin-depth limit in which the channel half-depth d satisfies $2d \ll 2\delta \approx \lambda$, where δ is half the diffusion length and λ is wavelength. For simplicity, the horizontal dimensions (x, y) are both scaled with h, and the thin-depth approximation is an asymptotic limit with $\varepsilon = d/h \ll 1$.

The governing equations are linearized by decomposing a general field variable q into its base state and perturbed state, $q = q_0 + q'$. Parallel flow base state (4.5) is assumed. The following scaling is adopted,

$$x, y \sim h,\ z \sim d,\ u_0 \sim U_{eo},\ t \sim h/U_{eo},\ \sigma_0 \sim \sigma_r, \tag{A 1a}$$

$$u', v' \sim U_{ev},\ w' \sim U_{ev}d/h,\ p' \sim \mu U_{ev}h/d^2,\ \phi' \sim E_a h,\ \sigma' \sim \sigma_r. \tag{A 1b}$$

Note that electric potential perturbation is scaled with h ($\sim O(\delta)$) because the perturbation is strongest at the conductivity interface.

After non-dimensionalization, the general variable is decomposed into $Q = Q_0 + Q'$ where Q_0 denotes non-dimensional base state, and Q' denotes non-dimensional perturbation. In the following derivation, capital letters denote non-dimensional variables. The linearized governing equations are

$$\varepsilon Pe\,(\partial_T \Sigma' + U_0 \partial_X \Sigma' + R_v(\partial_Y \Sigma_0)V') = \varepsilon^2 \partial_X^2 \Sigma' + \varepsilon^2 \partial_Y^2 \Sigma' + \partial_Z^2 \Sigma', \tag{A 2a}$$

$$\varepsilon^2 \Sigma_0^{-1}(\partial_X \Sigma' - (\partial_Y \Sigma_0)\partial_Y \Phi') = \varepsilon^2 \partial_X^2 \Phi' + \varepsilon^2 \partial_Y^2 \Phi' + \partial_Z^2 \Phi', \tag{A 2b}$$

$$\partial_X U' + \partial_Y V' + \partial_Z W' = 0, \tag{A 2c}$$

$$\begin{aligned}\varepsilon Re(\partial_T U' + U_0 \partial_X U' + (\partial_Y U_0)V') = &-\partial_X P' + \varepsilon^2 \partial_X^2 U' + \varepsilon^2 \partial_Y^2 U' + \partial_Z^2 U' \\ &-\Upsilon\left(\partial_X^2 \Phi' + \partial_Y^2 \Phi' + \varepsilon^{-2}\partial_Z^2 \Phi'\right),\end{aligned} \tag{A 2d}$$

$$\varepsilon Re(\partial_T V' + U_0 \partial_X V') = -\partial_Y P' + \left(\varepsilon^2 \partial_X^2 V' + \varepsilon^2 \partial_Y^2 V' + \partial_Z^2 V'\right), \tag{A 2e}$$

$$\varepsilon^2 \varepsilon Re(\partial_T W' + U_0 \partial_X W') = -\partial_Z P' + \varepsilon^2\left(\varepsilon^2 \partial_X^2 W' + \varepsilon^2 \partial_Y^2 W' + \partial_Z^2 W'\right), \tag{A2f}$$

where $Pe = U_{eo}d/D_{eff}$ is the Péclet number and $Re = \rho U_{eo}d/\mu$ is the Reynolds number; $R_v = U_{ev}/U_{eo}$ is the ratio of electroviscous to electro-osmotic velocities, and $R_v \sim O(1)$ in the regime of convective instability (see discussion in the main text). The coefficient in (A 2*d*) is $\Upsilon = L_d/\Gamma$, where $L_d = \delta/h \sim O(1)$ is the non-dimensional diffusion length. This coefficient in the electric body force term characterizes the effects of the diffusive conductivity profile, and $\Upsilon \sim O(1)$ for high conductivity ratios.

In the thin-depth limit ($\varepsilon \ll 1$), the leading-order terms of (A 2*b*) are

$$\begin{aligned}&\partial_Z^2 \Phi' = 0, \\ &\partial_Z \Phi'|_{Z=\pm 1} = 0,\end{aligned} \tag{A3}$$

where the homogenous Neumann boundary condition is due to non-penetrating walls. Hence,

$$\Phi' = \bar{\Phi}(X, Y). \tag{A4}$$

This means that the electric body force term in the momentum equation (A 2*d*) does not have Z-dependence at leading order.

In the thin-depth and low-Péclet-number ($\varepsilon Pe \ll 1$) limit, the leading-order terms of (A 2*a*) are

$$\begin{aligned} &\partial_Z^2 \Sigma' = 0, \\ &\partial_Z \Sigma'|_{Z=\pm 1} = 0. \end{aligned} \tag{A5}$$

Hence,

$$\Sigma' = \bar{\Sigma}(X, Y). \tag{A6}$$

In the thin-depth and low-Reynolds-number ($\varepsilon Re \ll 1$) limit, the leading-order terms of (A2*f*) are

$$\partial_Z P' = 0. \tag{A7}$$

Hence,

$$P' = \bar{P}(X, Y). \tag{A8}$$

The X- and Y-momentum equations, (A 2*d*)–(A 2*e*), reduce to

$$\begin{aligned} &\partial_Z^2 U' - \partial_X \bar{P} - \Upsilon \left(\partial_X^2 \bar{\Phi} + \partial_Y^2 \bar{\Phi}\right) = 0, \\ &U'|_{Z=\pm 1} = -R_v^{-1} U_0 \left(\partial_X \bar{\Phi} + n \Sigma_0^{-1} \bar{\Sigma}\right) = \bar{U}_{eo}, \end{aligned} \tag{A9}$$

$$\begin{aligned} &\partial_Z^2 V' - \partial_Y \bar{P} = 0, \\ &V'|_{Z=\pm 1} = -R_v^{-1} U_0 \partial_Y \bar{\Phi} = \bar{V}_{eo}, \end{aligned} \tag{A10}$$

where the velocity boundary condition is due to electro-osmotic flow (see (4.3)–(4.6)). The fact that $\bar{\Phi}$, $\bar{P}$ and $\bar{\Sigma}$ are all independent of Z suggests a solution by separation of variables of the form,

$$\boldsymbol{V}' = \bar{\boldsymbol{V}}_{ev}(X, Y) G(Z) + \bar{\boldsymbol{V}}_{eo}(X, Y), \tag{A11}$$

where $\boldsymbol{V} = U \boldsymbol{e}_X + V \boldsymbol{e}_Y$ represents velocity in the horizontal direction, and

$$G(Z) = 3/2(1 - Z^2). \tag{A12}$$

The coefficient 3/2 is chosen for later algebraic convenience.

The governing equations are produced by substituting the leading-order solutions, (A4), (A6), (A11), into the linearized equations (A 2). The Navier–Stokes equations (A 2*c*–*e*) are depth averaged in the following manner,

$$\bar{\boldsymbol{V}}(X, Y, T) = \tfrac{1}{2} \int_{-1}^{1} \boldsymbol{V}'(X, Y, Z, T) \, \mathrm{d}Z. \tag{A13}$$

Note the Z-component velocity W' disappears after depth averaging ($W'|_{Z=\pm 1} = 0$). The linearized governing equations reduce to

$$\varepsilon^{-1} Pe(\partial_T \bar{\Sigma} + U_0 \partial_X \bar{\Sigma} + R_v (\partial_Y \Sigma_0) \bar{V}) = \partial_X^2 \bar{\Sigma} + \partial_Y^2 \bar{\Sigma}, \tag{A14a}$$

$$\Sigma_0^{-1} (\partial_X \bar{\Sigma} - (\partial_Y \Sigma_0) \partial_Y \bar{\Phi}) = \partial_X^2 \bar{\Phi} + \partial_Y^2 \bar{\Phi}, \tag{A14b}$$

$$\partial_X \bar{U} + \partial_Y \bar{V} = 0, \tag{A14c}$$

$$\begin{aligned} &\varepsilon Re \left(\partial_T \bar{U} + U_0 \partial_X \bar{U} + (\partial_Y U_0) \bar{V}\right) \\ &\quad = -\partial_X \bar{P} + \varepsilon^2 \left(\partial_X^2 \bar{U} + \partial_Y^2 \bar{U}\right) - 3(\bar{U} - \bar{U}_{eo}) - \Upsilon \left(\partial_X^2 \bar{\Phi} + \partial_Y^2 \bar{\Phi}\right), \end{aligned} \tag{A14d}$$

$$\varepsilon Re (\partial_T \bar{V} + U_0 \partial_X \bar{V}) = -\partial_Y \bar{P} + \varepsilon^2 \left(\partial_X^2 \bar{V} + \partial_Y^2 \bar{V}\right) - 3(\bar{V} - \bar{V}_{eo}). \tag{A14e}$$

We have maintained the inertial terms and horizontal viscous terms in the momentum equations in order to keep the role of these forces in perspective. This approach is

similar to the Darcy–Brinkman–Forchheimer equation in porous media flow (see for example Liu & Masliyah 1996).

Appendix B. Governing matrices for linear stability analysis

The governing equations can be recast as a system of equations which are first order in X and T (see for example Schmid & Henningson 2001),

$$\partial_X \boldsymbol{\xi} = \mathscr{A}\boldsymbol{\xi} + \mathscr{B}\partial_T \boldsymbol{\xi}, \tag{B1}$$

where,

$$\boldsymbol{\xi} = (\bar{\Sigma}, \partial_X \bar{\Sigma}, \partial_X \bar{\Phi}, \partial_Y \bar{\Phi}, \bar{U}, \bar{V}, \partial_X \bar{V}, \bar{P})^T, \tag{B2}$$

and $\mathscr{A}$ and $\mathscr{B}$ are 8×8 matrix operators. $\mathscr{A}$ is a differential operator,

$$\mathscr{A} = \begin{pmatrix} 0 & 1 & 0 & 0 & 0 & 0 & 0 & 0 \\ -D^2 & \dfrac{PeU_0}{\varepsilon} & 0 & 0 & 0 & \dfrac{PeR_v \partial_Y \Sigma_0}{\varepsilon} & 0 & 0 \\ 0 & \dfrac{1}{\Sigma_0} & 0 & -D - \dfrac{\partial_Y \Sigma_0}{\Sigma_0} & 0 & 0 & 0 & 0 \\ 0 & 0 & D & 0 & 0 & 0 & 0 & 0 \\ 0 & 0 & 0 & 0 & 0 & -D & 0 & 0 \\ 0 & 0 & 0 & 0 & 0 & 0 & 1 & 0 \\ 0 & 0 & 0 & \dfrac{3U_0}{\varepsilon^2 R_v} & 0 & -D^2 + \dfrac{3}{\varepsilon^2} & \dfrac{ReU_0}{\varepsilon} & \dfrac{D}{\varepsilon^2} \\ -\dfrac{3n}{R_v}\dfrac{U_0}{\Sigma_0} & -\dfrac{L_d}{\Gamma}\dfrac{1}{\Sigma_0} & -\dfrac{3U_0}{R_v} & \dfrac{L_d}{\Gamma}\dfrac{\partial_Y \Sigma_0}{\Sigma_0} & \mathscr{A}_{85} & \mathscr{A}_{86} & -\varepsilon^2 D & 0 \end{pmatrix}, \tag{B3}$$

where D denotes differential operator in Y, and

$$\mathscr{A}_{85} = \varepsilon^2 D^2 - 3, \quad \mathscr{A}_{86} = \varepsilon Re(U_0 D - \partial_Y U_0).$$

$\mathscr{B}$ is an algebraic operator,

$$\mathscr{B}_{21} = \varepsilon^{-1} Pe, \quad \mathscr{B}_{76} = \varepsilon^{-1} Re, \quad \mathscr{B}_{85} = -\varepsilon Re; \quad \mathscr{B}_{pq} = 0 \ (p, q = \text{otherwise}). \tag{B4}$$

B.1. *Base state*

The base state conductivity profile is assumed to be one-dimensional. For a system with electrolytes of two conductivities σ_H and σ_L, with the reference conductivity $\sigma_r = (\sigma_H + \sigma_L)/2$ and conductivity ratio $\gamma = \sigma_H/\sigma_L$, the base conductivity profile is

$$\Sigma_0(Y) = 1 - \frac{2(\gamma - 1)}{\gamma + 1} \sum_{m=1}^{\infty} \frac{\sin\left(\frac{1}{2}(2m-1)\pi Y\right)}{\frac{1}{2}(2m-1)\pi} \exp\left(-(2m-1)^2 \pi^2 L_d^2/16\right). \tag{B5}$$

For a diffusion length smaller than the channel half-width (i.e. $L_d = \delta/h < 1/2$), this profile can be approximated very well by a solution that neglects reflections at walls (i.e. diffusion within an infinite medium) of the form,

$$\Sigma_0(Y) = \frac{2}{\gamma + 1} + \frac{\gamma - 1}{\gamma + 1} \operatorname{erfc}\left(\frac{Y}{L_d}\right). \tag{B6}$$

In fact, the differences in values computed using (B5) and (B6) are within 5×10^{-3} for $L_d \leqslant 0.5$.

The base velocity U_0 varies owing to the variation in base conductivity if $n \neq 0$ (as in (4.3)). In the non-uniform electro-osmotic flow case, U_0 must be a function of both Y and Z in order to be a solution to the Navier–Stokes equation ($\nabla^2 U_0 = 0$).

However, for $\delta/d = \varepsilon^{-1}L_d \geqslant 3$, it suffices to assume a one-dimensional base velocity as a first-order approximation.

B.2. *Boundary conditions*

The boundary conditions presented in this section apply to both spatial and temporal stability analysis outlined in § 5. The following boundary conditions are imposed at the walls ($Y = \pm 1$),

$$\partial_Y \bar{\Sigma} = 0, \tag{B7a}$$

$$\partial_Y \bar{\Phi} = 0, \tag{B7b}$$

$$\partial_Y \bar{U} = 0, \tag{B7c}$$

$$\bar{V} = 0, \tag{B7d}$$

Boundary conditions (B7*a*)–(B7*b*) are consequences of zero mass and electric fluxes at the walls, and (B7*c*)–(B7*d*) comprise the velocity boundary conditions for a Hele-Shaw type approximation. More specifically, (B7*d*) reflects a stationary wall, and (B7*c*) is derived from a zero-vorticity-perturbation condition at the wall. These velocity conditions are valid when the disturbances near walls are much smaller in magnitude than the disturbances near the conductivity interface (e.g. when $L_d \leqslant 0.5$). Four auxiliary boundary conditions are required for the 8×8 differential operator $\mathscr{A}$,

$$\partial_Y(\partial_X \bar{\Sigma}) = \partial_X(\partial_Y \bar{\Sigma}) = 0, \tag{B8a}$$

$$\partial_Y(\partial_X \bar{\Phi}) = \partial_X(\partial_Y \bar{\Phi}) = 0, \tag{B8b}$$

$$(\partial_X \bar{V}) = \partial_X(\bar{V}) = 0, \tag{B8c}$$

$$\partial_Y(\bar{P}) = \varepsilon^2 \partial_Y^2 \bar{V}, \tag{B8d}$$

where (B8*d*) is derived from the Y-component momentum equation (A14*e*).

Appendix C. Application of Briggs–Bers criteria

C.1. *Selection of physical modes*

Briggs' test is an excellent tool to distinguish physical modes from many spurious eigenvalues in the spatial stability analysis. This section briefly introduces the fundamental principle behind Briggs' test, and presents numerical continuation of physical eigenvalues as an application of Briggs–Bers criteria.

A convectively unstable system can be viewed as a noise amplifier, that is, a system in which a disturbance at the origin is amplified downstream (Briggs 1964; Bers 1983; Huerre & Rossi 1998). For a linearized system, the disturbance can be assumed to be temporally sinusoidal, i.e. with a component of the form $\mathrm{e}^{-\mathrm{i}\Omega T}$. Briggs and Bers proposed the following (Briggs') test to determine whether or not an amplifying wave solution (i.e. $-K_i > 0$, see § 5.1) is physical: if an imaginary component is added to the normally real frequency such that $\Omega_i > 0$, then any physical wave solution will become damped downstream (i.e. $-K_i < 0$) for cases where this added imaginary component is large enough. This test is based on the principle of causality (Briggs 1964): if a disturbance localized at the origin is growing very rapidly over time (i.e. with a large enough Ω_i), a system driven by this localized source will exhibit the largest disturbance at the origin; therefore, waves associated with this local disturbance decay downstream (i.e. with $-K_i < 0$). Briggs proved that a value of Ω_i greater than the maximum temporal growth rate is sufficient for such test. The temporal analysis from § 5.2 was employed to provide this limiting value of Ω_i.

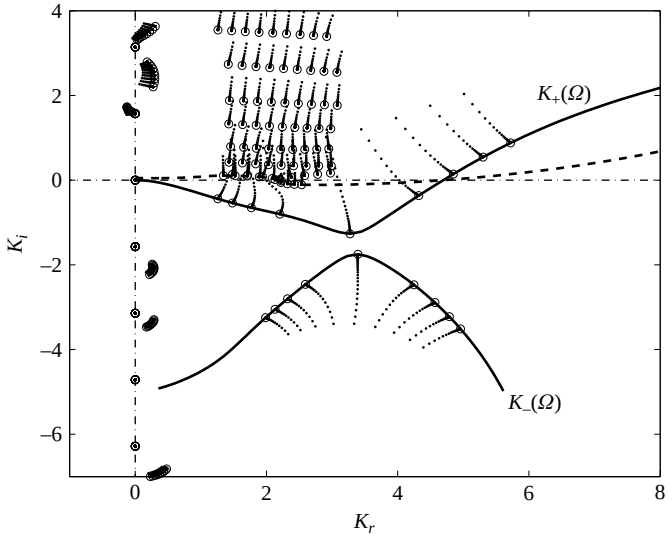

FIGURE 19. Selection of physical modes using Briggs' test. A gradually increasing positive Ω_i is added to each Ω which is initially real. The eigenvalues corresponding to the real Ω are denoted by circles, and eigenvalues corresponding to complex Ω are denoted by dots. One family of eigenvalues falls on the $K_+(\Omega)$ curve, which has a portion (below the real axis $K_i = 0$) satisfying the Briggs–Bers criteria. These eigenvalues correspond to physically amplifying waves and can be tracked through continuation, e.g. over gradually varying real Ω as in this plot. A family of evanescent waves is shown by another curve $K_-(\Omega)$. Multiple modes can be excited, e.g. another family of eigenvalues (dashed curve) also has a portion satisfying the Briggs–Bers criteria. Numerical parameters: $R_v = 4.89$ which is slightly below the onset of absolute instability; $\max(\Omega_i) = 0.50$ while the maximum temporal growth rate is 0.47; other parameters are described in table 2. Note only eigenvalue solutions (circles and dots) in the range $\Omega = 1.4$–3.0 are shown, but the continuation (solid and dashed curves) are for $\Omega = 0.0$–5.0.

Figure 19 shows the result of a sample Briggs' test. As Ω_i increases, one family of the eigenvalue solutions crosses the real axis (from $-K_i > 0$ to $-K_i < 0$) and satisfies the Briggs–Bers criteria, and is therefore a result of physical waves that grow downstream. Once physical roots are singled out at one set of parameters, a continuation procedure can be employed to track these physical eigenvalues by gradually varying the parameters. As an example, we show a continuation over frequency (see solid and dashed lines) in figure 19. Note that for certain parameter space, multiple roots can become physically unstable, and all of these must be tracked.

C.2. *Detection of absolute instability*

This section shows that the two methods for detecting absolute instability: identification using a saddle point and a cusp point in the eigenspectrum, respectively, provide equivalent results for our problem.

An absolutely unstable system can be viewed as an intrinsic oscillator in which the downstream propagating wave oscillates with an upstream propagating wave (Briggs 1964; Bers 1983; Huerre & Rossi 1998). Briggs and Bers proposed a method to identify absolute instability by the existence of a saddle point in the eigen-spectrum map resulting from Briggs' test. Physically, a saddle point corresponds to zero group velocity ($\partial\Omega/\partial K = 0$) for the unstable waves with maximum growth rate and therefore corresponds to absolute instability. Mathematically, the two solution branches $K_\pm(\Omega)$

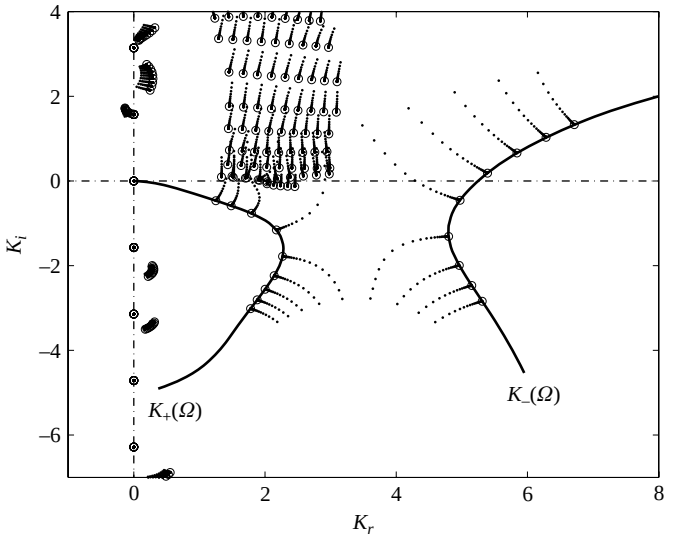

FIGURE 20. Identification of absolute instability: the cusp point detection in growth rate *vs.* frequency curve is verified by the saddle point in the Briggs map. The dotted lines are result of Briggs' test, among which a saddle point is evident. The solid curves are branch lines obtained through continuation, the fact that the branch lines interchange orientations compared to figure 19 confirms that there is one cusp point in each branch. The conditions are the same as figure 19 except that $R_v = 5.2$, which is above the threshold $R_{v,cr} = 4.9$ for absolute instability.

osculate at a certain frequency at which the group velocity is zero. If the saddle point occurs at $\Omega_i > 0$, the instability is absolute. This technique has been proved by rigorous complex analysis (Briggs 1964; Bers 1983). Huerre & Monkewitz introduced the Briggs–Bers criteria to the fluid mechanics community, and pointed out a cusp in $K_{\pm}(\Omega)$ (and osculation of both branches) is a warning for absolute instability (Huerre & Monkewitz 1985; Huerre & Rossi 1998).

The solid curves shown in figure 19 indicate a possible pinch of $K_+(\Omega)$ and $K_-(\Omega)$ if R_v is slightly higher. When the two branches osculate, there is a cusp point in growth rate versus frequency ($-K_i - \Omega$) curve (e.g. in figure 10*a*), which indicates absolute instability. This indication is confirmed by the saddle point in the Briggs map shown in figure 20. When velocity ratio R_v is higher than the onset of absolute instability, a saddle point is evident from the Briggs test. Compared to figure 19, the solution branches interchange orientations when R_v crosses $R_{v,cr}$, confirming the cusp indicated in figure 19. Because of its computational efficiency, we primarily used cusp point in the $-K_i - \Omega$ curve to identify absolute instability. The saddle-point detection using the Briggs test was applied to spot-check the validity of the absolute instability detected by a cusp point.

REFERENCES

ANDERSON, J. L. 1989 Colloid transport by interfacial forces. *Annu. Rev. Fluid Mech.* **21**, 61–99.

BAYGENTS, J. C. & BALDESSARI, F. 1998 Electrohydrodynamic instability in a thin fluid layer with an electrical conductivity gradient. *Phys. Fluids* **10**, 301–311.

BAZANT, M. Z., THORNTON, K. & AJDARI, A. 2004 Diffuse-charge dynamics in electrochemical systems. *Phys. Rev.* E **70**, 021506.

Bers, A. 1983 Space–time evolution of plasma insatbilities – absolute and convective. In *Handbook of Plasma Physics* (ed. A. A. Galeev & R. N. Sudan), chap. 3.2, pp. 451–517. North-Holland.

Briggs, R. J. 1964 *Electron-Stream Interaction with Plasmas*. MIT Press, Cambridge, MA.

Bruinsma, R. & Alexander, S. 1990 Theory of electrohydrodynamic instabilities in electrolytic cells. *J. Chem. Phys.* **92**, 3074–3085.

Chen, C.-H. 2004 Microscale electrokinetic transport and stability. PhD thesis, Stanford University.

Chen, C.-H., Lin, H., Lele, S. K. & Santiago, J. G. 2003 Electrokinetic microflow instability with conductivity gradients. In *Micro Total Analysis Systems* (ed. M. A. Northrup, K. F. Jensen & D. J. Harrison), pp. 983–987. Kluwer.

Chen, C.-H. & Santiago, J. G. 2002*a* Electrokinetic instability in high concentration gradient microflows. In *Proc. IMECE*, vol. 1. no. 33563.

Chen, C.-H. & Santiago, J. G. 2002*b* A planar electroosmotic micropump. *J. Microelectromech. Systems* **11**, 672–683.

Dang, F. Q., Zhang, L. H., Jabasini, M., Kaji, N. & Baba, Y. 2003 Characterization of electrophoretic behaviour of sugar isomers by microchip electrophoresis coupled with videomicroscopy. *Analyt. Chem.* **75**, 2433–2439.

Gaster, M. 1962 A note on the relation between temporally-increasing and spatially-increasing disturbances in hydrodynamic instability. *J. Fluid Mech.* **14**, 222–224.

Hoburg, J. F. & Melcher, J. R. 1976 Internal electrohydrodynamic instability and mixing of fluids with orthogonal field and conductivity gradients. *J. Fluid Mech.* **73**, 333–351.

Hoburg, J. F. & Melcher, J. R. 1977 Electrohydrodynamic mixing and instability induced by colinear fields and conductivity gradients. *Phys. Fluids* **20**, 903–911.

Horvath, A. L. 1985 *Handbook of Aqueous Electrolyte Solutions*. John Wiley.

Huerre, P. & Monkewitz, P. A. 1985 Absolute and convective instabilities in free shear layers. *J. Fluid Mech.* **159**, 151–168.

Huerre, P. & Rossi, M. 1998 Hydrodynamic instabilities in open flows. In *Hydrodynamics and Nonlinear Instabilities* (ed. C. Godrèche & P. Manneville), chap. 2, pp. 81–294. Cambridge University Press.

Hunter, R. J. 1981 *Zeta Potential in Colloid Science: Principles and Applications*. Academic.

Levich, V. G. 1962 *Physicochemical Hydrodynamics*. Prentice-Hall.

Lide, D. R. (ed). 1996 *Handbook of Chemistry and Physics*, 77th edn. CRC Press.

Lin, H., Storey, B. D., Oddy, M. H., Chen, C.-H. & Santiago, J. G. 2004 Instability of electrokinetic microchannel flows with conductivity gradients. *Phys. Fluids* **16**, 1922–1935.

Liu, S. J. & Masliyah, J. H. 1996 Single fluid flow in porous media. *Chem. Engng Commun.* **150**, 653–732.

Manz, A., Graber, N. & Widmer, H. M. 1990 Miniaturized total chemical-analysis systems – a novel concept for chemical sensing. *Sensors Actuators* B **1**, 244–248.

Matta, A., Knio, O. M., Ghanem, R. G., Chen, C.-H., Santiago, J. G., Debusschere, B. & Najm, H. N. 2004 Computational study of band crossing reactions. *J. Microelectromech. Systems* **13**, 310–322.

Melcher, J. R. 1981 *Continuum Electromechanics*. MIT Press, Cambridge, MA.

Melcher, J. R. & Schwartz, W. J. 1968 Interfacial relaxation overstability in a tangential electric field. *Phys. Fluids* **11**, 2604–2616.

Melcher, J. R. & Taylor, G. I. 1969 Electrohydrodynamics: a review of the role of interfacial shear stress. *Annu. Rev. Fluid Mech.* **1**, 111–146.

Newman, J. 1972 *Electrochemical Systems*. Prentice-Hall.

Oddy, M. H., Mikkelsen, J. C. & Santiago, J. G. 2001 Electrokinetic instability micromixing. *Analyt. Chem.* **73**, 5822–5832.

Pottel, R. 1973 Dielectric properties. In *Water: a Comprehensive Treatise* (ed. F. Franks), vol. 3, chap. 8, pp. 420–423. Plenum.

Probstein, R. F. 1994 *Physicochemical Hydrodynamics: An Introduction*, 2nd edn. John Wiley.

Ramsey, J. M. 2001 Preface. In *Micro Total Analysis Systems*. Kluwer.

Reyes, D. R., Iossifidis, D., Auroux, P. A. & Manz, A. 2002 Micro total analysis systems. 1. Introduction, theory, and technology. *Analyt. Chem.* **74**, 2623–2636.

Rubinstein, I. 1990 *Electro-Diffusion of Ions*. SIAM.

Santiago, J. G. 2001 Electroosmotic flows in micro-channels with finite inertial and pressure forces. *Analyt. Chem.* **73**, 2353–2365.

Saville, D. A. 1997 Electrohydrodynamics: the Taylor–Melcher leaky dielectric model. *Annu. Rev. Fluid Mech.* **29**, 27–64.

Schmid, P. J. & Henningson, D. S. 2001 *Stability and Transition in Shear Flows*. Springer.

Schrum, K. F., Lancaster, J. M., Johnston, S. E. & Gilman, S. D. 2000 Monitoring electroosmotic flow by periodic photobleaching of a dilute, neutral fluorophore. *Analyt. Chem.* **72**, 4317–4321.

Shultz-Lockyear, L. L., Colyer, C. L., Fan, Z. H., Roy, K. I. & Harrison, D. J. 1999 Effects of injector geometry and sample matrix on injection and sample loading in integrated capillary electrophoresis devices. *Electrophoresis* **20**, 529–538.

Swinney, K. & Bornhop, D. J. 2002 Quantification and evaluation of joule heating in on-chip capillary electropheresis. *Electrophoresis* **23**, 613–620.

Trefethen, L. N. 2001 *Spectral Methods in MATLAB*. SIAM.

Yao, S., Hertzog, D. E., Zeng, S., Mikkelsen Jr., J. C. & Santiago, J. G. 2003 Porous glass electroosmotic pumps: design and experiments. *J. Colloid Interface Sci.* **268**, 143–153.